



Skolkovo Institute of Science and Technology

Skolkovo Institute of Science and Technology

# AMBIENT POLARITONICS

*Doctoral Thesis*

by

ANTON PUTINTSEV

DOCTORAL PROGRAM IN PHYSICS

Supervisor

Director of Hybrid Photonics Labs, Professor Pavlos G. Lagoudakis

Co-Supervisor

Hybrid Photonics Labs, Dr. Denis Sannikov

Moscow - 2022

© Anton Putintsev, 2022.

I hereby declare that the work presented in this thesis was carried out by myself at Skolkovo Institute of Science and Technology, Moscow, except where due acknowledgement is made, and has not been submitted for any other degree.

Anton Putintsev

Prof. Pavlos G. Lagoudakis

# Abstract

For the last decades, substantial steps have been made towards utilizing the advantages of polariton physics for the usage in optical devices. Many exotic phenomena of bright physics have been observed in both organic and inorganic microcavities, but still, a lot of theoretical and experimental venues remain unexplored. While inorganic materials require cryogenic temperatures to be reached and defect-free structures to exhibit strong coupling with large polariton nonlinearities associated with polariton-polariton/exciton scattering, arising of state-of-the-art organic materials that exhibit outstanding optical properties allowing polariton physics at room temperature has made a leap forward towards bringing the field closer to its inorganic counterpart and to the point of consideration for practical applications. Though, copious technological, theoretical, and experimental challenges are still on the way.

The goal of this thesis is to explore the most relevant venues and demonstrate that ambient polaritonics does give a promise towards various applications. Hence, in this work, the author discusses firstly a study of polariton lasing in a  $\lambda/2$  planar strongly coupled organic microcavity filled with BODIPY-Br dye molecules and demonstrates the transition to a quasi-steady state, nanoseconds long-lived, single-mode polariton lasing regime. Secondly, the ability to undergo polariton condensation in a novel hybrid metal-DBR organic microcavity also filled with BODIPY-Br dye molecules is investigated with a concomitant comparison of a polariton condensation properties in a control DBR-DBR microcavity. At last but not least, second-order coherence properties of a room temperatures organic polariton condensates are examined where the author delineates an alternative approach to access second-order coherence that is based on well-controlled single-shot technique detection allowing for direct measurements of photon statistics of organic polariton condensates, demonstrates an extremely low excessive quantum noise of polariton photoluminescence reaching an experimentally measured value of  $g^2(0) = 1.00034$ , investigates nonlinear polariton system behavior upon reducing its lateral size, supported by a microscopic model that describes system dynamics, and studies stochastic and static disorder contributions to spatial filamentation of real-space polariton condensate profiles.

# Publications

## Main author

1. **A. D. Putintsev**, A. V. Zasedatelev, V. Y. Shishkov, M. Misko, D. Sannikov, E. S. Andrianov, Y. E. Lozovik, D. Urbonas, T. Stöferle, U. Scherf, R. F. Mahrt, and P. G. Lagoudakis, “Photon statistics of organic polariton condensates,” *under review in Physical Review X*
2. **A. D. Putintsev**, A. Zasedatelev, K. E. McGhee, T. Cookson, K. Georgiou, D. Sannikov, D. G. Lidzey, and P. G. Lagoudakis, “Nano-second exciton-polariton lasing in organic microcavities,” *Applied Physics Letters*, vol. 117, no. 12, p. 123302, 2020

## Co-author

1. K. E. McGhee, **A. D. Putintsev**, R. Jayaprakash, K. Georgiou, M. E. O’Kane, R. C. Kilbride, E. J. Cassella, M. Cavazzini, D. A. Sannikov, P. G. Lagoudakis, and D. G. Lidzey, “Polariton condensation in an organic microcavity utilising a hybrid metal-dbr mirror,” *Scientific Reports*, vol. 11, p. 20879, Oct 2021

*Dedicated to my parents.*

# Contents

<b>1</b>	<b>Introduction</b>	<b>10</b>
<b>2</b>	<b>Background</b>	<b>15</b>
2.1	History . . . . .	15
2.2	Strong-coupling . . . . .	16
2.3	Polariton condensation . . . . .	17
2.4	Organic polariton platforms . . . . .	21
<b>3</b>	<b>Quasi-steady state regime</b>	<b>23</b>
3.1	Overview and motivation . . . . .	23
3.2	Cavity design . . . . .	24
3.3	Condensation measurements . . . . .	25
3.4	Single-shot temporal dynamics . . . . .	28
3.5	Discussion . . . . .	31
<b>4</b>	<b>Hybrid organic microcavities</b>	<b>32</b>
4.1	Overview and motivation . . . . .	32
4.2	Hybrid distributed Bragg reflectors . . . . .	33
4.3	Optical properties of hybrid microcavities . . . . .	35
4.4	Condensation in metal-DBR microcavities . . . . .	41
4.5	Cavity homogeneity . . . . .	45
4.6	Discussion . . . . .	47
<b>5</b>	<b>Photon statistics of organic polariton condensates</b>	<b>50</b>
5.1	Overview and motivation . . . . .	50
5.2	Experimental setup design . . . . .	52
5.3	Cavity design . . . . .	54
5.4	Second-order coherence . . . . .	54
5.5	Spot-size analysis . . . . .	58
5.6	Integral emission properties . . . . .	63
5.7	Microscopic Model . . . . .	65
5.8	Numerical Simulations . . . . .	67
5.9	Discussion . . . . .	69
<b>6</b>	<b>Summary and outlook</b>	<b>71</b>
	<b>Bibliography</b>	<b>73</b>

# List of Figures

2-1	Matter-light coupling illustration. . . . .	16
2-2	Principle of a three-level Ruby laser operation. . . . .	18
2-3	Schematics of exciton-polariton condensation formation process via various relaxation channels. Adapted from Reference (4). . . . .	19
2-4	Organic materials as foundation for ambient polariton platforms . . . .	22
3-1	(a) Cavity design and (b) its angle-dependent reflectivity spectra . . .	25
3-2	(a) Reflectivity map and (b) real-space photoluminescence . . . . .	26
3-3	Spectral characteristics of the polariton emission . . . . .	27
3-4	Time-resolved single-shot photoluminescence measurements . . . . .	30
4-1	Hybrid metal-DBR mirrors. . . . .	34
4-2	(a) Normalised absorption (red) and photoluminescence (blue) spectra of BODIPY-Br at 10% by mass in polystyrene. The molecular structure is shown in the inset. Schematic of (b) the hybrid Ag-DBR microcavity and (c) a conventional DBR-DBR microcavity. . . . .	35
4-3	Cavity design and pumping/detection configuration in reflection . . .	36
4-4	The effect of the number of hybrid mirror pairs on microcavity optical properties. . . . .	37
4-5	Electric field simulations of the cavity mode (red) and refractive index (blue) for (a) the 1-pair hybrid cavity, (b) the 5-pair hybrid cavity, and (c) the DBR-DBR control cavity. From this, it can be seen that the penetration length of the E-field changes in the different mirrors. Here, we omit the top DBR mirror as it is the same for all cavities, and thus the x-axis denotes the distance from the interface between the top DBR and the active layer. The different layers are shaded for clarity. Adapted from Reference (3). . . . .	38
4-6	The effect of the number of hybrid mirror pairs on microcavity optical properties. . . . .	39
4-7	Experimental setup for single-shot measurements in reflection configuration . . . . .	41
4-8	Hallmarks of organic polariton condensation in a hybrid metal-DBR microcavity . . . . .	42
4-9	Hallmarks of organic polariton condensation in the control DBR-DBR microcavity . . . . .	43
4-10	Hallmarks of organic polariton condensation in the control DBR-DBR microcavity . . . . .	46

4-11	Hallmarks of organic polariton condensation in the control DBR-DBR microcavity . . . . .	47
5-1	Experimental setup for single-shot measurements . . . . .	52
5-2	Cavity structure and pumping configuration . . . . .	54
5-3	Polariton number distributions and Fano factor . . . . .	55
5-4	Zero-time-delay second-order correlation function . . . . .	56
5-5	Real-space, k-space, and dispersion images. $g_2(0)$ vs Pump power . . . . .	58
5-6	Spot-size dependencies of threshold, blueshift, and linewidth . . . . .	60
5-7	Polariton group velocity distribution from the dispersion imaging . . . . .	61
5-8	Polariton weighted group velocity dependence on spot-size . . . . .	61
5-9	Bottom left figure shows dependencies of the calculated $g^{(2)}(0) - 1$ values at zero time-delay at $\sim 2P_{th}$ as a function of Region of Interest (ROI) size within which the real-space polariton intensity is integrated for different spot-sizes of the condensate: $14\mu m$ , $22\mu m$ , $24\mu m$ , $34\mu m$ , $39\mu m$ , and $44\mu m$ . Each point of each curve is averaged over 8 different positions on the sample, and error bars represent the spread. Right figure demonstrates dependence of the second-order coherence function at zero time-delay at $\sim 2P_{th}$ as a function of an excitation spot size corresponding to cross section values along red dashed line from left panel. Top insets visualize ROI masks applied to real-space profile of a $44\mu m$ condensate. . . . .	63
5-10	Polariton emission s-curves for different spot-sizes from experiment and model . . . . .	64
5-11	Model s-curves for different: (a) Radiative losses constants and (b) different thermalization constants . . . . .	67
5-12	Evolution of thermalization term in rate equations fro transitions from higher energy states to the ground energy state for two different values of polariton losses . . . . .	68
5-13	Evolution of thermalization term in rate equations fro transitions from higher energy states to the ground energy state for two different values of polariton losses . . . . .	69

## Glossary

**SK** Skolkovo Institute of Science and Technology

**PL** Photoluminescence

**BEC** Bose-Einstein Condensate

**LP** Long-pass edge filter

**SP** Short-pass edge filter

**DMLP** Single-edge laser Dichroic Mirror Long-pass

**NA** Numerical Aperture

**ND** Neutral Density filter

**PD** Photo detector

**CW** Continuous Wave

**FWHM** Full Width at Half Maximum

**EMCCD** Electron Multiplying Charge-Coupled Device

**UPB** Upper Polariton Branch

**MPB** Middle Polariton Branch

**LPB** Lower Polariton Branch

**DBR** Distributed Bragg Reflectors

**TDAF** ter(9,9-diarylfuorene)

**PLQY** Photoluminescence Quantum Yield

**BODIPY-Br** Brominated Boron Dipyrromethene dye dispersed in a Polystyrene matrix

**MeLPPP** Methyl-substituted Ladder-type Polymer Poly(Paraphenylene)

# Chapter 1

## Introduction

Polaritons are quasi-particles formed as a result of the strong interaction of light with matter (excitons and photons), which have an integer spin and, as a result, obey Bose-Einstein statistics. Being hybrid particles, they inherit the properties of both components: a small effective mass ( $10^{-4} - 10^{-5}$  electron mass) and a short lifetime (10 ps) from the photon component and strong nonlinear properties from the exciton component. Strong interaction is realized inside heterostructures called microresonators and conventionally consisting of two distributed Bragg reflectors and an active medium in between them. The study of polariton physics at room temperature became possible not so long ago, thanks to modern equipment and techniques for creating microresonators on the nanometer scale using organic materials as the active medium of such structures. The localized nature of Frenkel excitons excited in organic materials allows them to remain stable without the need to reach cryogenic temperatures, since their binding energy exceeds the thermal motion energy of molecules  $kT$ , which makes it possible to observe the phenomenon of strong coupling between light and matter under normal conditions. The first Bose-Einstein condensation of such particles was observed in inorganic microresonators at a temperature of 4K during the interaction of Wannier-Mott excitons and photons by Kasprzak et al. (5), while the first room temperature polariton laser was demonstrated by Kena-Cohen et al. (6). Recently, polaritonics succeeded in various optical devices such as an optical amplifier, optical transistor, and even all-optical logic (7; 8).

Though, in order to compete with conventional laser devices, one of the most essential steps is to bring the idea of maintaining CW-lasing operation in organic systems within our reach. This would certainly add up coherence to the field of ambient polaritonics, bolster up the interest in conducting studies in that direction, and potentially could pave the way towards implementation of the devices based on connected polariton condensates, allowing, in principal, all-optical polariton circuitry on a chip. So far, there has been no demonstration of such a regime in strongly coupled organic systems. For this reason, demonstration of quasi-steady state exciton-polariton lasing/condensation in organic systems is a one of the central parts of this thesis.

However, a gentle nature of organic materials exploited for ambient polaritonics renders it as an extremely difficult task to find appropriate conditions to create and maintain such quasi-steady state environment in a system intrinsically dissipative by nature and highly prone to photodegradation. Each of the available platforms for ambient polaritonics such as molecular dyes, polymers, fluorescent proteins, organic crystals and organic/inorganic perovskites, has either advantages or disadvantages, an ideal candidate has not yet been found in terms of the stability, resistance to photobleaching, and strong nonlinearity. Moreover, an essential step in pushing the field to its most compelling shores is studying novel designs of microcavities and creation of microresonators: the choice of materials and the number of pairs for creating Bragg mirrors, the presence of additional layers inside the resonator to prevent photooxidation, the additional spacers to adjust the position of the active medium with respect to the maximum field inside the resonator to ensure maximum coupling between the field and matter with nanometer precision. In this regard, the author explores the possibility of exploiting Hybrid metal-DBR mirror in organic microcavities for studying Frenkel exciton-polariton physics. The hybridity of the structure consists in the use of an aluminum mirror as a substrate for the lower DBR, as a result of which the structure becomes completely opaque in the wavelength range under study. The advantage of such hybrid resonators is the relative ease of fabrication compared to similar DBR-DBR structures and the expected reduction in lasing threshold. The complexity of the study lies in the necessity to implement an

experimental setup operating in a reflective configuration operating in a single-shot excitation regime. To date, exciton/polariton condensation has not been demonstrated in such structures, which makes this part of the work of a highly relevance in the field and beyond.

Further, macroscopic quantum phenomena in exciton-polariton systems have for a long time been the subject of an extensive research going far beyond purely fundamental interest. In a similar way shot-noise of lasers defines limits for laser cooling and precise interferometry, noise in polariton systems sets boundaries for emerging polariton applications such as organic polariton transistors, single-photon polariton switches, electrically pumped polariton lasers, exciton-polariton topological insulators, and polaritonic neuromorphic computing. However, gentle organic materials used for ambient polaritonics make it an extremely cumbersome task to study statistical properties of the condensate emission due to intrinsic tendency to photodegradation and necessity to sustain millions of pump pulses without altering emission properties. Moreover, high thermal fluctuations and strong spatial disorder drastically sophisticate their theoretical study, while on the experimental side their sub-picosecond polariton dynamics cannot be acquired by standard Hanbury Brown and Twiss (HBT) measurements due to the insufficient time resolution of single-photon avalanche photodetectors of  $\sim 40ps$ . Hence, until now, second-order coherence and photon statistics of room-temperature polariton condensates remain an unexplored territory.

Throughout the last part of the thesis, the author develops an alternative approach to access second-order coherence which is based on well-controlled single-shot detection allowing for direct measurements of photon statistics of polariton condensates. Similar approaches relying on single photodetector measurements have been used previously to study second order coherence in atomic condensates. Using this technique, we demonstrate an unexpectedly low excessive quantum noise of around 1.9% for spatially highly fragmented organic polariton BECs at room temperature. Reducing the size of the system increases the condensation threshold, nonlinearities, and effective polariton thermalization rate due to kinetic losses originated from ballistic propagation of polaritons out of the condensate area. However, it does

not reduce the degree of fragmentation in a condensate, but instead enhances the shot-to-shot fluctuations, while studied in a single-shot excitation regime.

In the following I list the flow of information through the structure of the thesis:

**Chapter 2 - Background** Here's the literature review. Introduction to an underlying physical phenomena attributed to polariton physics, and overview of organic materials suitable for polariton applications at ambient conditions.

**Chapter 3 - Quasi-steady state regime** In this chapter I discuss and investigate a quasi-steady state, 1.2 nanoseconds long-lived, single-mode polariton lasing in organic microcavity filled with BODIPY-Br dye molecules and study concomitant spectral changes in polariton emission. I then discuss prospects and valuable insights this work may lead to.

**Chapter 4 - Hybrid metal-DBR organic microcavities** I then jump to the investigation of optical properties, fabrication peculiarities, advantages and drawbacks, and overall competitiveness for polariton applications of a new organic microcavity hybrid design where instead of two Distributed Bragg Reflectors (DBRs) we utilize metal-DBR microcavities to observe exciton polariton condensation.

**Chapter 5 - Photon statistics in organic microcavities** In this chapter I investigate quantum statistical properties of polariton condensates in organic active media. My experimental study demonstrates low particle number fluctuations for highly populated condensates at room temperature. I show a quantum noise of the condensate of  $\sim 100$  times the shot-noise-limit of an ideal coherent light source setting up the lower limit of the noise for organic polariton devices. I delineate peculiar behaviour in second-order coherence function once the system size is changed. Therefore a thorough analysis of how dynamical, spectroscopic, and coherent properties of organic polariton depend on the size of the lateral system is carried out.

**Chapter 6 - Summary and outlook** In the last chapter, we discuss our results in the broader field's scope, how they contribute to and broaden it, and what

promises they give for future polaritonics operating at ambient conditions.

"Things are as they are because they were as they were."

Thomas Gold

## Chapter 2

# Background

### 2.1 History

A subject of investigation to modern science is not only real particles such as molecules, atoms, ions, all sorts of fermions, neutrinos, that exist freely in nature and are stable in time, but also so-called quasi-particles, or collective excitations which arise when we consider a sophisticated macroscopic system to behave as it contains various weakly, or strongly, interacting particles in vacuum. For instance, interaction between electrons and holes in semiconductors can be described in terms of elementary excitations called excitons, which are essentially a bound state between electron and a hole attracted to each other by an electrostatic Coulomb interaction. This is in high contrast to organic semiconductors, where elementary excitations are also present, but are called Frenkel excitons, and their nature is a result of a weak, electrostatic van der Waals forces that confines the material into a solid state. Hence in organic materials excitons are tightly bound or highly localized states with a characteristic size of  $\sim 10\text{\AA}$ , while in inorganics they are identified as Wannier–Mott states with a characteristic size of  $\sim 100\text{\AA}$  that allows them to travel easier across a crystal lattice.

A cavity-polariton (from now on just polaritons) is a quasiparticle formed by coupling an exciton to a confined photon mode within an optical cavity. Cavity-polaritons are bosons and have an effective mass of  $\sim 10^{-11}$  that of an atom (9) and therefore undergo Bose–Einstein condensation (BEC) at temperatures much higher

than those observed with atomic gases (10). In this process, polaritons condense into a single state once their density reaches a certain critical threshold, with all polaritons within the condensate having the same energy, momentum, and phase. Photons emitted by the condensate share these properties and as such possess the same characteristics as a laser (11). This type of emission has been termed polariton lasing (4; 12; 13; 14), with these devices being of emerging interest as novel low-threshold lasers and light-sources.

## 2.2 Strong-coupling

Polaritons are hybrid quasi-particles that arise when elementary excitations of the medium confine strongly with electromagnetic radiation - a regime known as strong light-matter coupling. In this case, the normal modes of the system are not separate light and matter excitations anymore but instead become hybrids, with properties inherited from both their matter and light constituents. This regime can be reached when an active medium, or absorber, is placed in a high finesse microcavity.

Many microcavities are based on two distributed Bragg reflectors (DBRs) placed either side of the active layer. Such DBRs generally consist of a stack of alternating high- and low- refractive index quarter-wave layers, producing mirrors that possess both high reflectivity  $> 99\%$  and low optical absorption. In a Fabry-Pérot microcavity, the reflectivity of the cavity mirrors directly controls the degree of optical confinement and the cavity mode linewidth. Optical confinement can be defined by the cavity quality-factor (Q-factor) that is expressed using  $Q = \lambda/\Delta\lambda$ , where  $\lambda$

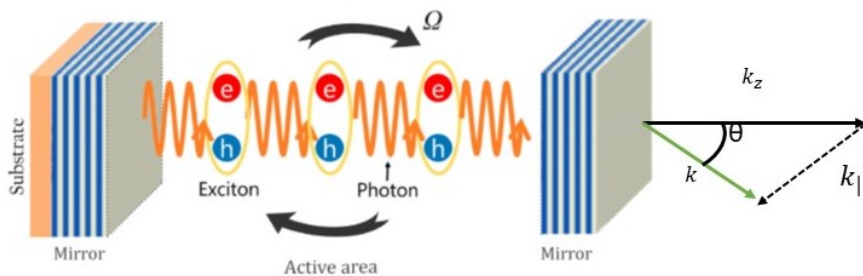


Figure 2-1: Microcavity structure and matter-light coupling illustration. Two DBRs with an active material sandwiched in between.

is the cavity mode wavelength and  $\Delta\lambda$  is its spectral full-width at half maximum (FWHM) (15). Hence, by controlling cavity finesse that defines sharpness of the cavity resonance and by controlling inhomogeneous broadening of excitons in active material that defines scattering rate of excitons we can reach a regime when total losses of both cavity photons,  $\gamma_{ph}$  and excitons,  $\gamma_{exc}$ , are less than coupling strength between them. Then strong coupling is reached.

There are different theoretical approaches to derive new hybridized eigenstates of the system. The most trivial one considers single-photon coupling to a two-level system, and it is the Jaynes–Cummings model with the system Hamiltonian as follows:

$$H = w \hat{\mathbf{a}}^\dagger \hat{\mathbf{a}} + E \sigma^+ \sigma^- + g(\sigma^+ \hat{\mathbf{a}} + \hat{\mathbf{a}}^\dagger \sigma^-) \quad (2.1)$$

where  $\sigma^\pm$  are Pauli matrices describing raising and lowering transitions between states in a two level system with the energy  $E$ , and  $\hat{\mathbf{a}}^\dagger$  and  $\hat{\mathbf{a}}$  are creation and annihilation operators for photon. The last term describes a coherent coupling between the electromagnetic field and exciton with a coupling strength  $g$ . For a fixed number of photons and excitons,  $n_{ex}$  in the system, the expression (2.1) can be expressed in a  $2 \times 2$  matrix and diagonalized to find new eigenvalues of the system:

$$H_{n_{ex}} = n_{ex}w + \begin{pmatrix} e - w & g\sqrt{n_{ex}} \\ g\sqrt{n_{ex}} & 0 \end{pmatrix}, E_{n_{ex}}^\pm = (n_{ex}-1)w + \frac{1}{2} \left[ E + w \pm \sqrt{(E - w)^2 + 4g^2 n_{ex}} \right] \quad (2.2)$$

We will discuss this model in a bit more detail further in Chapter 5, as it was used as grounds to develop upon to describe experimental results on photon statistics in organic polariton condensates.

## 2.3 Polariton condensation

Before we dive into a discussion on how we should relate to the phenomenon of polariton macroscopic occupation of a ground energy state and differentiate between

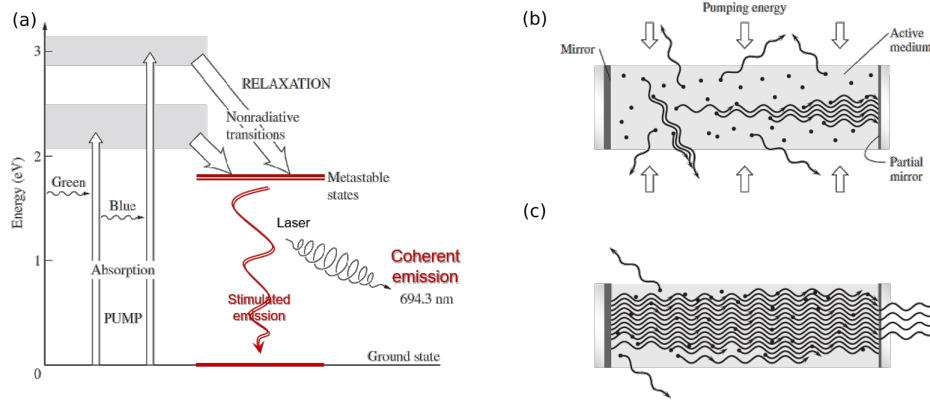


Figure 2-2: (a) Energy level schematic of a three-level Ruby laser system. (b), (c) Two regimes of photon emission process for a conventional laser: spontaneous and stimulated emission. Adapted from Reference (16).

exciton-polariton lasing, condensation, or Bose-Einstein condensation, lets take a step back and delineate polariton lasing and how it is conceptually different from conventional photon lasing.

In normal lasers we pump the system by means of optical or electrical pumping to excite active material to higher energy states from where via a non radiative relaxation transitions it can occupy a long-living meta-stable state with a life-time of up to milliseconds, Fig2-2a. From there the system can relax and spontaneously emit photons in all directions, Fig2-2b. But when the pumping rate is increased and a lasing threshold is reached, a population inversion on this meta-stable state with respect to the ground state occurs, and the first few spontaneously radiated photons stimulate a chain reaction resulting in a stimulated emission into a photon mode. During this stimulated emission process a coherent monochromatic light is emitted, Fig2-2b, or lasing.

Now, in strongly coupled systems, energy is stored in a form of hybridized form of matter excitations and electromagnetic field - polaritons. And rather than emission, one should discuss various scattering processes from dark excitonic reservoir. Because once the system scattered into a polariton state, it simply decays from a microcavity within the polariton lifetime. Relaxation processes in the system can be divided into two main subgroups. The first subgroup is responsible for populating polariton states, upper or lower ones, from high energy exciton reservoir.

into bright polaritonic states, Fig2-3 In inorganic semiconductors these relaxation processes are mainly the interaction with high energy optical phonons (17), and electron polariton scattering (18). For organic semiconductors it is either vibron assisted radiative pumping (19) or phonon mediated non-radiative scattering (20). But once excitons have relaxed to polariton states, thermalization processes step in, and, due to different nature of excitons, they are not the same in organic and inorganic materials. While nonlinear interactions with low frequency molecular vibrations (21) are responsible for thermalization in organic materials, interactions with acoustic phonons or free charges (22) and polariton-polariton scattering (23) governs thermalization mechanisms in inorganic materials.

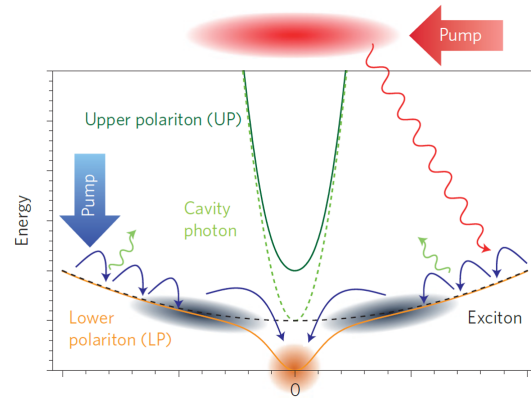


Figure 2-3: Schematics of exciton-polariton condensation formation process via various relaxation channels. Adapted from Reference (4).

Once the exciton reservoir becomes more and more populated by means of an increasing non-resonant optical pumping, for instance, more and more polaritons start to occupy a ground state, and at some point stimulated relaxation to the ground polariton state dominates other relaxation channels. This is when the build up of a coherent macroscopically occupied state occurs, Fig2-3. And this state is called exciton-polariton condensation. Up to this point no coherent emission in the system, or any lasing, have taken place as only non-radiative and radiative relaxation processes of energy conversion inside the system were considered. And coherence, polarization, momentum, and phase are all the properties of a macroscopic wavefunction that describes a condensed state preoccupied by polaritons. But due to dissipative nature of the system, polaritons have a finite life-time, and so does the polariton condensation. And dissipating, the system, or cavity, can spontaneously emit photons. These leaking photons inherit the phase, polarization, momentum, and energy of this macroscopic wavefunction, and are called the polariton lasing.

Hence, the source of a coherent emission in a polariton system is a spontaneous decay of a coherent, macroscopically occupied state. That is what makes the main difference from conventional lasing.

In recent years, increasing attention has been shown to the exploration of polariton condensation effects in organic semiconductor microcavities, (6; 24; 25; 26; 27). Here, Frenkel excitons have a binding energy that is much greater than  $k_B T$  at room temperature (28) and thus organic exciton–polariton microcavities are able to undergo room temperature condensation (9; 6; 24).

Lets now briefly discuss the part why it is common to interchangeably use terms polariton lasing and polariton condensation, and why it is not entirely accurate to call it a Bose-Einstein condensation, even though it is widely accepted in the community. Since polaritons are composite quasi-particles, i.e. a superposition between exciton and photon, they are bosons as they have an integer spin (1 from photon and 1 from exciton that itself is a sum of half-spin electron and a hole) and hence, they could in principle undergo a transition to a Bose-Einstein Condensation (BEC). Textbook physics defines a BEC as a macroscopically occupied state which is macroscopically occupied by a gas of Bose particles, where the density of these particles is high enough for them to reduce their chemical potential to the ground state. In general, for a particle in 3-dimension with a dispersion relation given by  $E_k = \hbar^2 k^2 / 2m$  we can write BEC distribution as follows:

$$n = \int \frac{d^3 k}{(2\pi)^3} \frac{1}{\exp(E_k \mu - k_B T) - 1} \quad (2.3)$$

The critical density is reached when  $\mu \rightarrow 0$  and  $n(\mu \rightarrow 0) = (mk_B T / 2\pi \hbar^2)^{3/2} \zeta(3/2)$ , where  $\zeta(3/2) \approx 2.61$  is the Riemann zeta function, and when particle density exceeds this value, macroscopic fraction of particles occupies lowest energy state. The above holds for non-interacting Bose gas. In 2-dimensions, though, (2.3) diverges as  $\mu \rightarrow 0$  and, hence, condensed state is not achievable for any given temperature or density. However, if we consider an interacting Bose gas in two dimensions, it can undergo a phase transition to a low temperature order state, which is called Berezinskii–Kosterlitz–Thouless transition, but not a BEC (29).

## 2.4 Organic polariton platforms

So far, polariton condensation has been achieved in a wide spectrum of organic materials. Even though first works on organic microcavities were aimed mainly at J-aggregate cyanine dyes in host matrices (31; 32; 33), first polariton condensation was observed in an organic single crystal (24).

Then, the most studied materials for polariton applications are fluorene oligomer TDAF (an ambipolar blue organic light-emitting diode material (34)), brominated boron dipyrromethene dye dispersed in a polystyrene matrix (BODIPY-Br), extensively studied by Cookson et al. 2017(35) and was used to demonstrate quasi-steady state regime for polariton lasing (2), which is also a part of this thesis and will be extensively discussed in Chapters 3 and 4. Another nonbrominated boron dipyrromethene (BODIPY-G1) dye was utilized to investigate blueshift and polarization properties in polariton condensate (27), and recently a highly photostable fluorescent dye 1,4-bis[2-[4-[N,N-di(ptolyl) amino]phenyl]vinyl]benzene (DPAVB) dispersed in a transparent polymer matrix (36) was shown to demonstrate a strong-coupling regime and undergo transition to a polariton condensate sustaining more than  $> 37000$  pulses at  $2P_{th}$ .

Conjugated polymers to some degree combine properties of molecular dyes and organic crystals, and methyl-substituted Ladder-type polymer poly(paraphenylene) (MeLPPP) was the first organic material to be spin coated and exhibit polariton condensation being embedded in a dielectric microcavity (9). In our Hybrid Photonics Laboratory in Skoltech I utilized this particular material to study photon statistic in organic polariton condensate, and we will extensively discuss it further in Chapter 5. Moreover, fluorescent proteins that can be biologically derived have recently been attracting a huge interest and have also been utilized to observe polariton condensation. For instance, jellyfish *Aequorea victoria* (37) possesses green fluorescent proteins (GFP) which were cloned and were found of a considerable interest in fluorescent microscopy. Polariton lasing was observed with GFPs as active medium (38) as well as with another fluorescent protein mCherry (39). The molecular structures of different organic materials are shown in Fig2-4.

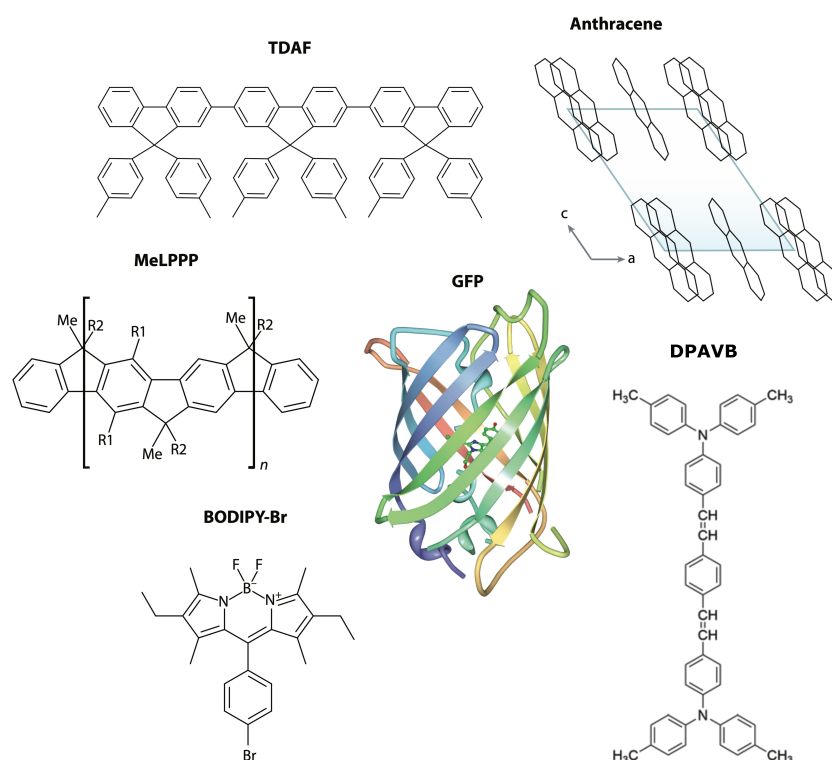


Figure 2-4: Set of organic materials exhibiting polariton condensation. Abbreviations: Anthracene crystal structure; TDAF, ter(9,9-diarylfuorene); MeLPPP, methyl-substituted Ladder-type polymer poly(paraphenylene); GFP, green fluorescent proteins; BODIPY-Br, brominated boron dipyrromethene; DPAVB, 1,4-bis[2-[4-[N,N-di(p-tolyl) amino]phenyl]vinyl]benzene. Adopted from reference (30).

"Time is what keeps everything from happening at once."

Ray Cummings

## Chapter 3

# Quasi-steady state regime

### 3.1 Overview and motivation

Strongly coupled organic microcavities are perhaps the most developed material systems for ambient polaritonics. A broad range of suitable materials has enabled the experimental observation of polariton lasing across the whole visible range (6; 9; 24; 38; 35; 40; 41; 42; 43; 44; 27), as well as device-concepts ranging from ultra-fast transistors and all-optical logic gates (44; 45), to single-photon switching (46), all at room temperature under ambient conditions. However, the localised nature of Frenkel excitons, alongside the typically ultra-short polariton lifetimes,  $\sim 100fs$ , limit both the study of many-body phenomena and applications that require macroscopic polariton transport. Unlike the case of inorganic semiconductor microcavities, where continuous wave (CW) excitation allows for the replenishment of particle losses, leading to the realisation of steady state polariton condensates, in organic semiconductors polaron formation and photobleaching hinders CW operation. In a recent study, quasi-steady operation was implemented using nanosecond non-resonant optical excitation in multi- $\lambda$  fluorescent protein microcavities (38) that led to the observation of extended temporal coherence, reaching  $150ps$  (39), i.e. 3 orders of magnitude longer than the corresponding cavity lifetime. Multi- $\lambda$  cavities host several consecutive cavity modes complicating the distinction between strong and weak coupling regimes. Here, we use a single-mode  $\lambda/2$  strongly coupled microcavity of a BODIPY dye molecule. BODIPY dyes have been the subject of extensive

studies for their applications in the strong coupling regime (47). Strongly coupled BODIPY microcavities (48; 49; 50) and polariton lasing in these structures allow for highly monochromatic tuneable coherent emission of duration up to  $\simeq 2$  picoseconds (35; 41; 27).

In this first experimental chapter, the author demonstrates quasi-steady state polariton lasing in a single-mode  $\lambda/2$  strongly coupled BODIPY microcavity, namely the nanosecond long-lasting polariton condensate which exceeds inherent ultrafast polariton lifetime ( $\sim 100$  fs) by 4-orders of magnitude. I employ a single-shot dispersion, real-space imaging, and time-resolved photoluminescence (PL) technique that allows for full characterisation of the polariton condensate emission and its transient PL dynamics under a single excitation pulse, where each excitation pulse-amplitude and spatial profile are simultaneously recorded. The aforementioned technique prevents averaging of the polariton emission characteristics due to pulse-to-pulse intensity fluctuations ( $\sim 15\%$  for nanosecond YAG pumped optical parametric amplifiers) and photo-bleaching of the organic emitter.

## 3.2 Cavity design

The microcavity structure under investigation consists of a  $\lambda/2$ -thin organic slab based on BODIPY-Br dye molecules dispersed into polystyrene host as 1:10 by mass that, in turn, is sandwiched between two distributed Bragg reflectors (DBR). For the bottom mirror, a 10-pair  $\text{Nb}_2\text{O}_5/\text{SiO}_2$ - DBR was deposited onto a quartz-coated glass substrate using a mix of ion-assisted electron beam deposition and thermal evaporation with the deposition rate of 10Å/s. The BODIPY-Br/PS solution was spin-coated on top with an approximate thickness of 183 nm. A second DBR consisting of 8 pairs of  $\text{Nb}_2\text{O}_5/\text{SiO}_2$ -  $\lambda/4$  layers was deposited on top of the spin-coated organic material with the rate of 2Å/s, using an electron beam without an ion gun to avoid damage of organics. The microcavity has a Q-factor of  $\sim 450$ , supporting strong light-matter coupling between the cavity photon and the Frenkel exciton resonance associated with singlet  $S_{0,0} - S_{1,0}$  electronic transition centered at 2.34 eV as shown on the right panel of Figure 3-2a. Reflectivity spectra is present

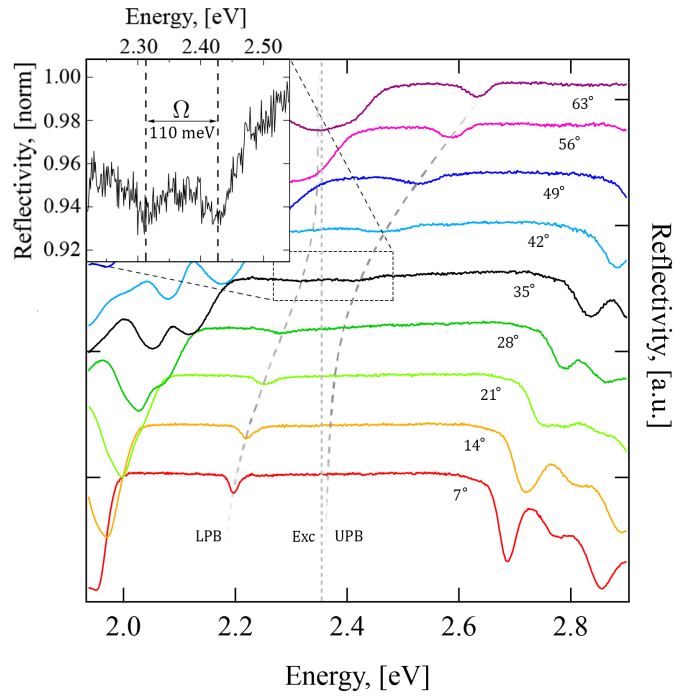


Figure 3-1: Angle-dependent reflectivity spectra of the microcavity recorded at different angles exhibit clear anti-crossing at the exciton resonance energy  $E_{exc}$  (gray dotted-line) that occurs at  $k_{||} = 6\mu m^{-1}$  and indicates the formation of lower (LPB, gray dashed-line) and upper (UPB, gray dashed-line) exciton-polariton branches. The inset shows the reflectivity spectrum recorded at 35 degree of incidence that corresponds to  $k_{||} = 6\mu m^{-1}$ .

on Fig.3-1 for a set of different angles.

### 3.3 Condensation measurements

The reflectivity map in Figure 3-2a that demonstrates anti-crossing of the bare exciton and cavity modes at  $k_{||} = 6\mu m^{-1}$  ( $35^\circ$ ) with a well-resolved normal mode splitting of 110 meV (inset graph of Figure 3-2a). By fitting the data using a coupled oscillator model we extract the value of Rabi splitting ( $\Omega$ ) equal to 110 meV that agrees well with the mode splitting at the anti-crossing point and fulfils criteria for the strong coupling regime(51) according to  $\Omega > \sqrt{2(\gamma^2 + \kappa^2)} = 85$  meV, where  $\gamma = 60$  meV and  $\kappa = 2.5$  meV are bare exciton and photon linewidths (half widths at half maximum).

The author performed an optical excitation of the microcavity using 4ns sin- gular pulses tuned at the first Bragg minimum of the reflectivity spectrum (462nm)

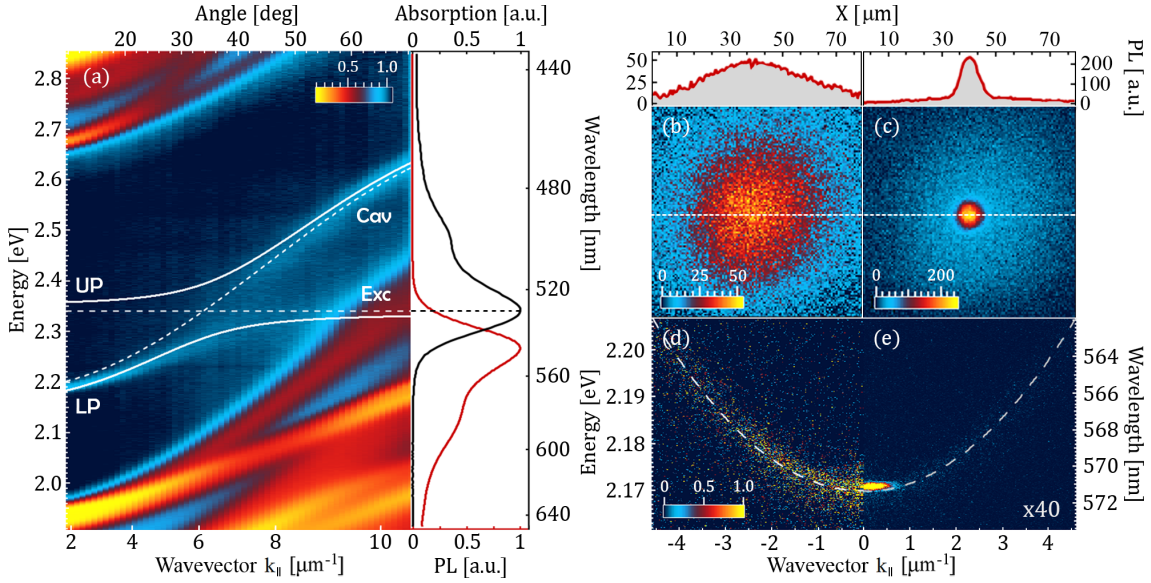


Figure 3-2: (a) Angularly resolved reflectivity map of the microcavity showing the anti-crossing of the bare exciton and cavity modes (Exc, Cav, white dashed curves) at  $k_{||} = 5\mu\text{m}^{-1}$ . The white solid lines are the calculated upper (UP) and lower (LP) polariton branches for a vacuum Rabi-splitting of  $110\text{meV}$  and  $-164\text{meV}$  exciton-photon detuning. The inset graph shows reflectivity spectrum at the anti-crossing point  $k_{||} = 6\mu\text{m}^{-1}$  ( $35^\circ$ ) taken along the white vertical dashed line. The right panel shows the absorption (black) and photoluminescence (red) of the neat BODIPY-Br film. (b), (c) Single-shot real-space photoluminescence images showing the spatial distribution of polariton density under a single non-resonant nanosecond excitation pulse below and above condensation threshold, respectively. The top panels show the respective cross-section of the photoluminescence at the position of the dashed white lines. (d), (e) Single-shot dispersion imaging of the  $E, k_{||}$ -distributions of polariton density below and above the condensation threshold respectively. The white dashed lines show the position of the lower polariton branch and the solid lines the angularly integrated photoluminescence. Adapted from Reference (2).

in order to reduce sample heating. Then, single-shot real-space images and  $E, k_{||}$ -distributions of polariton PL were recorded in the transmission configuration. Figure 3-2b shows a typical linear polariton PL real-space image at  $P = 0.75\text{MW}/\text{cm}^2$ ; the cross-section along  $x$ -axis has the same full width at half maximum (FWHM) as the pump spot ( $40\mu\text{m}$ ). With increased pump power by a factor of  $\sim 2$  ( $P = 1.7\text{MW}/\text{cm}^2$ ) the spatial distribution shrinks substantially ( $8\mu\text{m}$  in FWHM), as shown in Fig.3-2c, and the emission intensity increases nonlinearly. Figures 3-2d,e are single-shot dispersion images showing the polariton PL distribution along the lower polariton branch (LPB), for the two pumping intensities. At low pump power, polariton PL is distributed along the LPB, while for  $\sim$  twice the pump power we

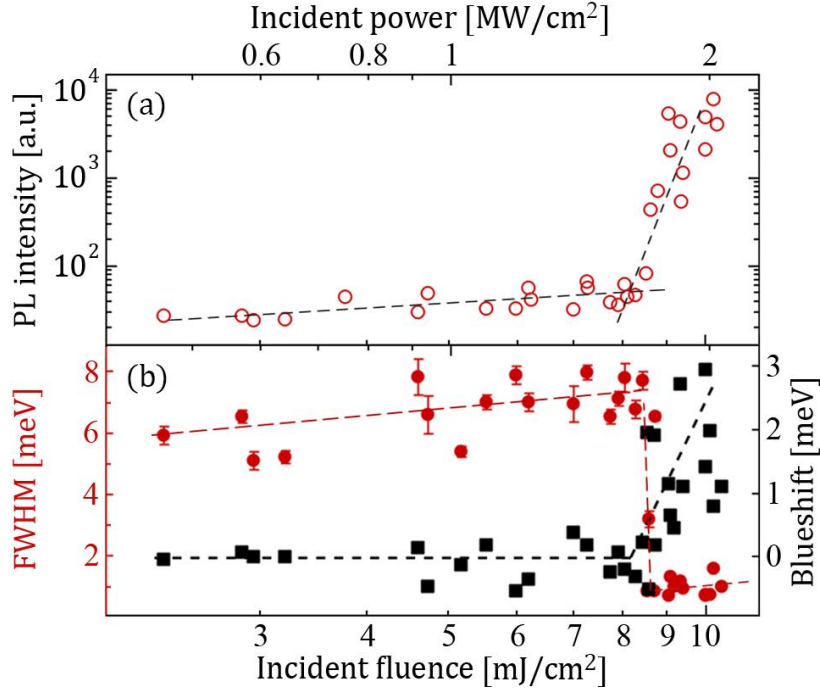


Figure 3-3: (a) Polariton photoluminescence intensity at  $k_{\parallel} \sim 0$  integrated into the range over  $\pm 0.2 \mu\text{m}^{-1}$  as the function of incident pump fluence (bottom axis), incident pump power density (top axis). The crossing point of the black dashed lines is used to define condensation threshold. (b) The linewidth of polariton photoluminescence at FWHM (solid red circles) and the energy shift of the lower polariton mode at  $k_{\parallel} = 0$  (solid black squares) versus incident pump fluence (bottom axis) and incident pump power density (top axis). The dashed lines are guides to the eye. Adapted from Reference (2).

observe a collapse of the polariton distribution at the ground polariton state. The white line profiles show the angularly integrated PL evidencing strong linewidth narrowing and an energy blueshift at the higher pump power. These spectroscopic characteristics are indicative of polariton condensation in semiconductor microcavities (9; 24; 38; 35; 40; 43; 41; 42; 44; 27). Next we perform a full pump fluence dependence to resolve the threshold excitation density for polariton condensation.

For the next step, I implement and conduct a single-shot dispersion imaging for a range of pump fluences. Figure 3-3a,b show the pump-power dependencies of PL intensity, linewidth, and blueshift at the ground polariton state  $k_{\parallel} = 0$ . One can explicitly see a clear threshold of the emission intensity at an incident pump fluence of  $P_{th} = 8 \text{ mJ/cm}^2$  within  $\pm 0.05 P_{th}$  variation across a few  $\text{mm}^2$  sample area indicating good uniformity of the structure. This value is almost coincides

with the threshold ( $6mJ/cm^2$ ) under 2ps-short pulsed excitation(41). The observed condensation threshold is equivalent to  $1.5MW/cm^2$  in terms of irradiance - the conventional parameter for the quasi-CW excitation; comparing thresholds in inorganic and hybrid organic-inorganic systems operating under quasi-CW pumping at room temperature(52; 53), it requires  $\sim 50$  - *times* higher pump power. The threshold is defined as the intersection point of linear and nonlinear curves fitting the PL intensity, shown in Fig.3-3a by dashed lines. Note: we restrict the range of pump fluences to avoid any possible degradation of the structure. At threshold pump fluence we observe a 7-fold reduction in linewidth from 7 meV to 1 meV and a concomitant blueshift of the ground polariton state up to 3 meV, as shown in Fig.3-3b red and black data, respectively. We believe the condensate linewidth of 1 meV is the result of inhomogeneous broadening due to dynamic blueshift. Recently, it was shown the blueshift arises from the interplay of the saturation effects and intermolecular energy migration of both: bright and dark molecules(27). These spectroscopic characteristics together with the spatial collapse of the polariton emission provide strong experimental evidence for the formation of a polariton condensate under nanosecond optical excitation. Interestingly, we find that the spectral properties of polariton condensates under nanosecond excitation are in quantitative agreement with previous studies using picosecond excitation pulses (35; 41). It remains therefore to resolve the temporal dynamics of the emission and identify whether the duration of the condensate extends substantially beyond the polariton lifetime.

### 3.4 Single-shot temporal dynamics

To investigate temporal dynamics, single-shot time-resolved PL measurements using a silicon photodiode with  $0.5ns$  rise-time are performed. Figure 3-4a shows the normalized intensity of the temporal profile of a typical pump pulse (blue dashed line), the instrument response function (IRF) (black dotted line), and polariton PL (red solid line) averaged over five pulses to improve signal-to-noise ratio. For convenience,  $0ns$  time is defined at the beginning of IRF's rising edge. The IRF is limited to  $\simeq 1.03ns$  at FWHM and the excitation pulse has a duration of  $\simeq 4ns$  at

FWHM. The polariton PL is collected within the whole numerical aperture of the microscope objective ( $NA = 0.42$ ). Below threshold, at  $P \simeq 0.5P_{th}$  the temporal profile of polariton PL follows the pump pulse, extending to  $\simeq 5.5ns$  at FWHM. The dominant process populating polariton states is intracavity radiative pumping as follows from the extensive study of polariton population mechanisms in such dye-filled microcavities(48). It implies an effective population of polariton states through the radiative decay of fluorescent dyes inside the cavity. Therefore, the lifetime of the exciton reservoir governs relaxation dynamics of polariton PL below the threshold and defines time delay of about 1ns with respect to the pump profile accordingly. It agrees well with the typical PL decay time of bare BODIPY-Br films (47). Since the energy difference between exciton reservoir and the ground polariton state is equal to 164meV one can also anticipate contribution from vibronic relaxation channel(54; 55; 56; 44). Figure 3-4b shows a single-shot spatial profile of polariton PL for one of the pulses included in the average of the temporal polariton PL profile of Figure 3-4a. Figure 3-4c shows the original and deconvoluted temporal profiles of the normalised polariton PL for pump fluence twice above the threshold ( $P \simeq 2 \times P_{th}$ ) with respect to the pump pulse.

We can observe a shortening of the rise time of polariton PL above threshold, resolution limited by the IRF, revealing the rapid formation of the condensate due to bosonic stimulation of carriers from the exciton reservoir to the ground polariton state. The condensate lifetime defined as the duration of deconvoluted polariton PL at FWHM is equal to  $\simeq 1.2ns$ , that exceeds polariton lifetime by a factor of  $\sim 10000$ . Indeed, the lifetime of lower polaritons at the ground state can be assessed as  $1/\tau_{LP} = |X|^2/\tau_{Exc} + |C|^2/\tau_C = 94fs$ , where  $\tau_{Exc} = 1/\pi\gamma = 22fs$  is the effective exciton dephasing time – inverse proportional to the linewidth of the matter component (it is an upper limit of the dephasing rate as being assessed from the inhomogeneously broadened electronic transition  $S_{0,0} - S_{1,0}$ );  $\tau_C = Q/2\pi\nu_C = 136fs$  is the photon lifetime in the cavity with given  $Q = 450$  and bare mode energy of  $E_C = 2.175meV$  ( $\nu_C = 526THz$ );  $|X|^2 = (1 + \delta/\sqrt{(\delta^2 + \Omega^2)})/2 = 0.085$  and  $|C|^2 = (1 - \delta/\sqrt{(\delta^2 + \Omega^2)})/2 = 0.915$  are exciton and cavity photon fractions of the ground polariton state. Figure 3-4d shows the corresponding single-shot spatial condensate

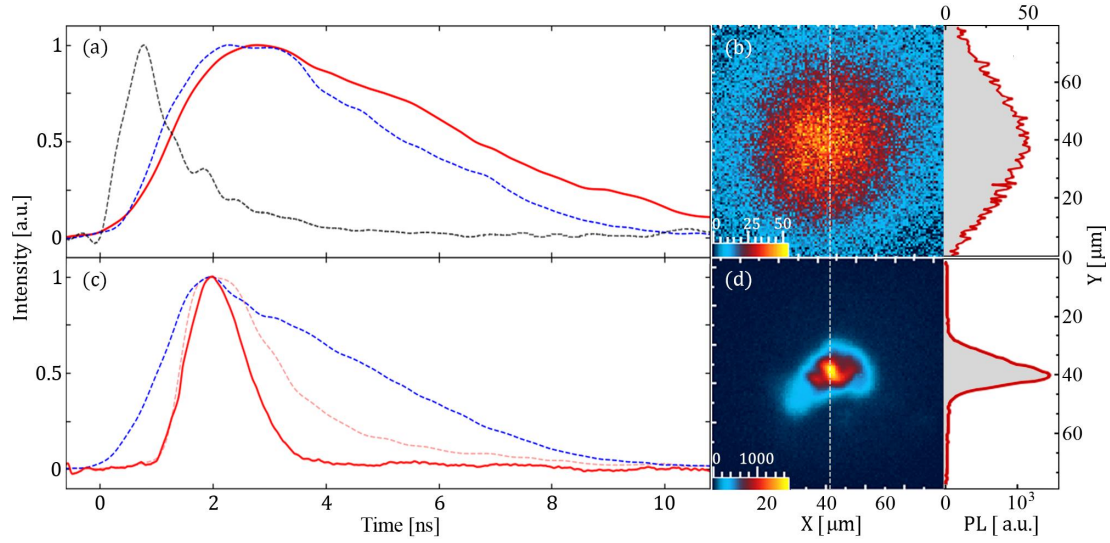


Figure 3-4: (a) Normalized, time-resolved polariton photoluminescence intensity (red solid line) below condensation threshold, averaged over five realisations/pulses. The blue dashed line shows the temporal profile of a single excitation pump pulse, and the black dashed line corresponds to the instrument response function (IRF) of the detector. (b) Single-shot real-space polariton photoluminescence image below condensation threshold. (c) Single-shot, normalized, time-resolved polariton photoluminescence intensity (red dashed line) at approximately twice the condensation threshold and its deconvolution with IRF (red solid line). The blue dashed line corresponds to the normalized single-shot pump pulse profile. (d) Single-shot real-space polariton photoluminescence image at approximately twice the condensation threshold. The right panels of (b,d) show the profile of the photoluminescence intensity at the position of the vertical white dashed line. Adapted from Reference (2).

profile, which has collapsed below the spatial extent of the excitation pulse. The collapse originates from the nonlinear increase of PL at the area within the pump profile, where the optical gain exceeds losses. Asymmetries in the condensate profile presumably relate to the effect of energy disorder inherent to organic microcavities. The small spatial distribution of the condensate reduces dynamical instabilities in agreement with previous studies(57; 58). Comparison of the spatial PL profiles of Figures 3-4b,d provide supporting evidence that the temporal profile of Fig.3-4c

corresponds to the emission from a polariton condensate. The temporal dynamics of polariton PL above condensation threshold provide a unique direct observation of a quasi-steady state polariton condensate in a  $\lambda/2$  planar organic microcavity.

## 3.5 Discussion

The direct measurement of the condensate lifetime provides valuable insight on the transient processes of nonequilibrium polariton condensation, its connection with spectral and polarization properties (27), dynamical instabilities, and noise limits of coherent polariton sources (58). The latter study elucidates the crucial role of a condensate lifetime with respect to the Bogoliubov instability time-scale on the onset of domain formation in a condensate wavefunction that dictates whether it possesses homogeneous or highly disordered spatial distribution. Moreover, characterization of the condensate lifetime facilitates the understanding of complex nonlinear dynamics, including rates of depletion and replenishment of the exciton reservoir and polariton states, respectively, under pulsed excitation (27). Long-lasting condensates exceeding polariton lifetime for several orders of magnitude push the system one step closer towards the regime of dynamic equilibrium as it corresponds to quasi-steady state operation regime in view of ultrafast dynamics inherent to strongly-coupled organic microcavities. This regime allows one to investigate hydrodynamics of polaritons (59), including room-temperature superfluidity (60) and interactions between separate condensates (61) that are capable of flowing over sufficient distances within the condensate lifetime. Realisation of nanosecond organic polariton condensates offers the possibility for devices relying on connected polariton condensates, paving the way for all-optical polariton circuitry on a chip (62; 63; 7; 64; 65), available now in ambient conditions (44; 46; 45).

"If I have seen further than others,  
it is by standing upon the shoulders  
of Giants."

Isaac Newton

## Chapter 4

# Hybrid organic microcavities

### 4.1 Overview and motivation

In this chapter, we address the issue of time-consuming, costly, and prone to error fabrication process of conventional DBR-DBR microcavities, and explore a new type of ‘hybrid’ dielectric mirror that is composed of a thick layer of a metal (Ag) onto which we deposit one or more dielectric mirror pairs. Here, the function of the silver mirror is to provide a high, broadband optical reflectivity that is then enhanced by a low number of DBR pairs, with such structures being significantly easier to fabricate. We are going to characterise the properties of these hybrid mirrors and show that a structure composed of 4 DBR pairs backed by a silver film have a comparable reflectivity to that of a conventional 10-pair DBR. We then will investigate the properties of strongly-coupled cavities made using a hybrid mirror, an organic semiconductor dye, and a conventional DBR, and show that cavities incorporating a 1-pair hybrid mirror have a Rabi splitting energy that is around 14% larger than a 9-pair/10-pair DBR–DBR control. We also demonstrate enhanced confinement, with structures based on a 10-pair hybrid mirror having a Q-factor that is 24% larger than the DBR control. We then explore the non-linear properties of a cavity utilising a 1-pair hybrid mirror and show that it can undergo polariton-condensation. However, we find in contrast to the DBR control cavity, emission from the hybrid cavity does not fully coincide with the bottom of the lower polariton branch. Using atomic force microscopy (AFM) and scanning electron microscopy

(SEM), we show that this effect most likely results from disorder at the interface between the Ag mirror and the DBR.

Lets briefly delineate particularities of fabricating process and associated issues with conventional microcavities. Many organic semiconductors have been shown to enter the strong coupling regime using microcavities with relatively low-reflectivity mirrors. Despite the fact that photon mode linewidths in low Q-factor cavities are relatively large (10-100 meV), the high oscillator strength of organic semiconductors results in large Rabi splitting energies,  $\hbar\Omega_{Rabi}$ , of 100's of meV to  $\sim 1eV$  (66; 67; 68; 69). Many of the highest Rabi splittings using organic semiconductors have been observed in structures based on two metallic reflectors (at least one of which is semi-transparent) with Q-factors of 10–65 (66; 70; 71; 72; 73). Here, the small optical penetration depth of metals such as silver (Ag) results in a high degree of optical confinement, which reduces the effective cavity length ( $L_{eff}$ ). As the Rabi splitting is inversely proportional to  $L_{eff}$ , ‘all metal’ cavities are generally characterised by increased Rabi splittings, and—as they are simple to fabricate via thermal evaporation—have effectively become the structure of choice in which to explore polaritonic properties that do not rely on non-linear effects (25; 70; 71). To achieve polariton condensation, however, relatively extended polariton lifetimes are required. Most exciton–polariton microcavities that have been reported to undergo condensation are based on two DBR mirrors and typically have Q-factors of several hundred to  $> 1000$  (41; 74; 75). The reflectivity of a DBR strongly depends on the number of dielectric pairs (15), and thus such mirrors often comprise in excess of 30 individual layers, (35; 76; 77). Hence, fabricating such structures once again is time-consuming, costly, and prone to error process.

Let us now discuss the design of hybrid distributed Bragg reflectors.

## 4.2 Hybrid distributed Bragg reflectors

Hybrid metal-DBR mirrors we fabricated by thermally evaporating a 200nm Ag film onto a quartz-coated glass substrate, followed by the deposition of various numbers (between 1 and 10) of  $SiO_2/Nb_2O_5$  quarter-wave pairs (refractive index  $\sim 1.46$  and

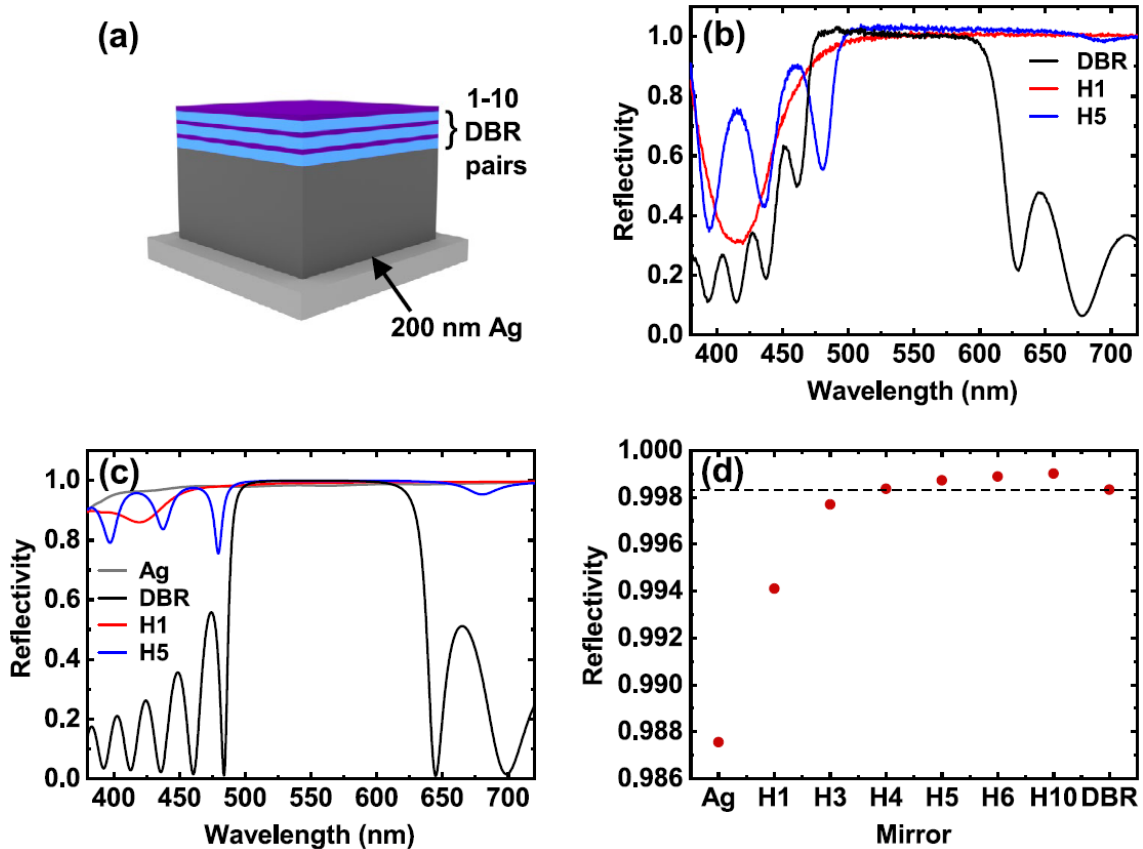


Figure 4-1: Hybrid metal-DBR mirrors. (a) Schematic of hybrid mirror. (b) Shows the experimentally measured reflectivity of the 1-pair hybrid (red), 5-pair hybrid (blue) and 10-pair DBR (black) mirrors, with transfer matrix reflectivity data for the same mirrors plus Ag (grey) shown in (c). (d) Plots the calculated reflectivity of each mirror at 550 nm. The horizontal dashed black line corresponds to the reflectivity of a 10-pair DBR. In (b–d), legend and x-axis labels ‘HX’ correspond to the hybrid mirrors, where X is the number of DBR pairs on top of the Ag, and ‘Ag’ and ‘DBR’ correspond to an Ag film and the 10-pair DBR, respectively. Adapted from Reference (3).

$\sim 2.20$ , respectively) by electron beam evaporation. The structure of such a hybrid mirror is shown schematically in Fig.4-1a. Figure 4-1b shows the normal incidence white light reflectivity of a 1-pair hybrid, 5-pair hybrid and 10-pair (conventional) DBR mirror, with a 200nm Ag mirror used as a reference. Figure 4-1c plots the reflectivity determined using a transfer matrix reflectivity (TMR) model for the same three mirrors and also that of silver. Here, our structures are based on a relatively thick silver film (200nm) to maximise its optical reflectivity. Our TMR model indicates that the reflectivity of a silver film does not increase once its thickness exceeds 200nm. The cavity structures that we use (for details see Section 4.3

"Optical properties of hybrid microcavities") are designed to extract light through a conventional 'top' DBR, and thus our approach allows us to use relatively thick silver films having high reflectivity and low optical transmission on the bottom mirror. We can see from Fig.4-1c that the hybrid mirrors have a comparable reflectivity to a conventional DBR, together with a significantly broader stopband (high-reflectivity region) resulting from the use of a silver mirror. Indeed, our TMR simulations indicate that the hybrid mirrors (except for the 1-pair hybrid) have a reflectivity that is ( $> 99.5\%$ ) over a bandwidth of  $130\sim 140\text{nm}$  (corresponding to  $\sim 530\text{meV}$ ). This high-reflectivity band is wider than the stop-band of the control DBR, which is limited to around  $90\text{ nm}$  ( $\sim 350\text{meV}$ ). This widened stop-band is potentially useful, as the large oscillator strength of organic semiconductors can result in large Rabi splittings ( $100\text{'s}$  of  $\text{meV}$ ) that are often greater than the width of the stopband of a conventional DBR. Figure 4-1d plots the TMR model reflectivity of each mirror explored (Ag, hybrid, DBR) at  $550\text{nm}$ . It can be seen from this that, at this wavelength, hybrid mirrors with five or more pairs have increased reflectivity compared to a 10-pair DBR.

### 4.3 Optical properties of hybrid microcavities

We have used the hybrid mirrors outlined in Fig.4-1 to fabricate a series of strongly-coupled microcavities containing the molecular dye bromine-substituted boron-dipyrromethene

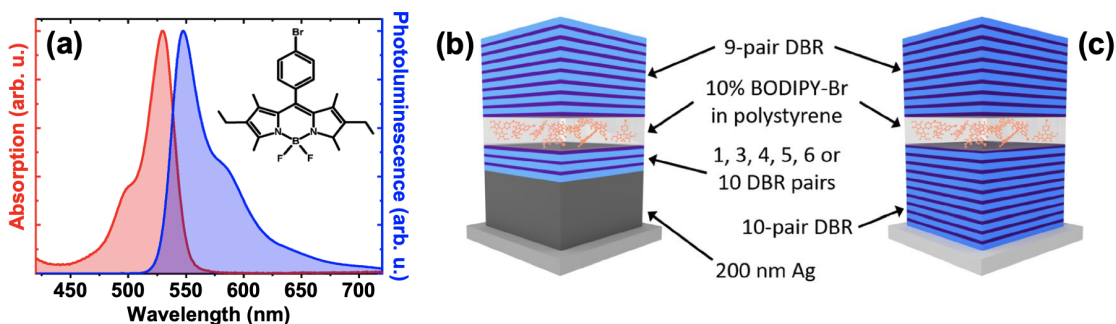


Figure 4-2: (a) Normalised absorption (red) and photoluminescence (blue) spectra of BODIPY-Br at 10% by mass in polystyrene. The molecular structure is shown in the inset. Schematic of (b) the hybrid Ag-DBR microcavity and (c) a conventional DBR-DBR microcavity. Adapted from Reference (3).

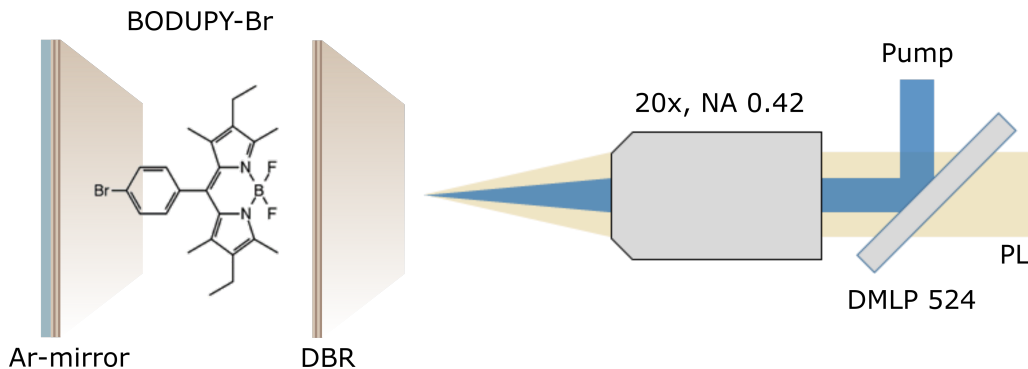


Figure 4-3: Cavity design and pumping/detection configuration in reflection.

(BODIPY-Br). This dye combines high oscillator strength and relatively high photoluminescence quantum yield, and has previously been shown to undergo polariton-condensation (35; 2). Additionally, its photoluminescence (PL) emission lies in a spectral region not easily accessible with traditional inorganic semiconductors (green/yellow), making it desirable for laser applications.

To process BODIPY-Br it was first dispersed into a polystyrene (PS) matrix at 10% by mass in toluene. Here, the function of polystyrene is to prevent molecular aggregation, a process that results in the quenching of BODIPY-Br luminescence. To create thin films, the BODIPY-Br/PS blend was deposited by spin-coating. Figure 4-2a shows the normalised absorption and PL spectra of a BODIPY-Br/PS film on a quartz substrate, with the molecular structure of BODIPY-Br shown in the inset. It can be seen that the absorption and PL peak around  $530\text{nm}$  and  $547\text{nm}$ , respectively.

Microcavities were fabricated by spin-coating a BODIPY-Br/PS solution onto the hybrid-DBR mirrors. This was followed by the deposition of a 9-pair DBR (via e-beam evaporation) on top of the active layer to create the full structure as shown in Fig.4-2b. In all cases, the thickness of the BODIPY-Br/PS layer was chosen to give a cavity mode positioned around  $547\text{nm}$ . As a control, we also fabricated a DBR–DBR cavity with a 10-pair bottom DBR, an active BODIPY-Br/PS layer, and a 9-pair top DBR. The structure of this cavity is shown in Fig.4-2c. To characterise the cavities, we first performed angle-dependent white light reflectivity measurements to confirm they operated within the strong coupling regime. Here, measurements were performed using a goniometer setup in which

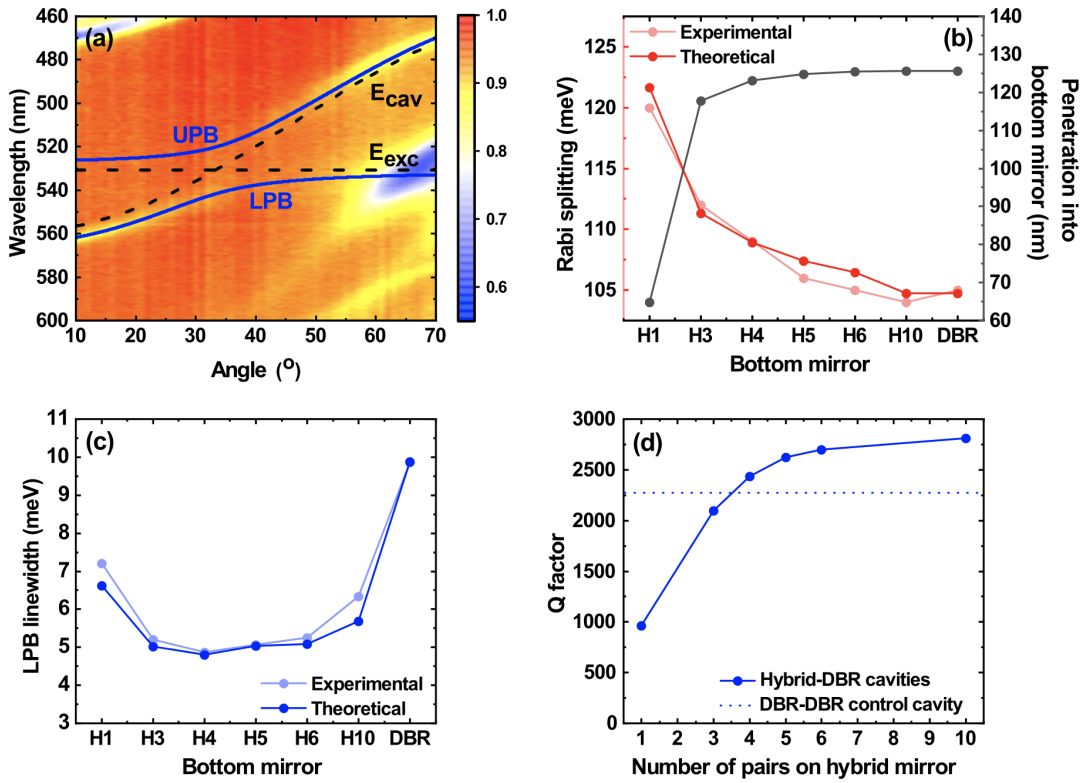


Figure 4-4: (a) Plots the angle-dependent reflectivity measurement of a 4-pair hybrid mirror cavity. Fits of upper (UPB) and lower (LPB) polariton branches (blue solid lines) are made using a standard two-level oscillator model. The dispersion of the cavity photon mode ( $E_{cav}$ ) and the exciton energy ( $E_{exc}$ ) are also shown (black dashed lines). (b) Shows the Rabi splitting for the hybrid mirror cavities and the DBR control, where good agreement can be seen between experimental (light red, two-level oscillator) and theoretical (dark red, TMR) values. The modelled penetration of the electromagnetic field into the bottom mirror (grey) is also shown here. (c) Shows the linewidth of the LPB for the hybrid mirror and DBR cavities, comparing experimental (light blue) and theoretical (dark blue, from TMR) values. In both (b) and (c), the x-axis labels ‘HX’ correspond to the hybrid mirrors, where X is the number of DBR pairs on top of the Ag, and ‘DBR’ corresponds to the 10-pair DBR. In (d), we plot the modelled Q-factor for hybrid mirror cavities with cavity mode at 547 nm. The modelled Q-factor of the DBR control cavity is indicated by a horizontal blue dotted line. Adapted from Reference (3).

a lens system positioned on a rotating optical rail was used to focus unpolarised white light onto the cavity surface. A series of lenses on a second rotating optical rail were used to collect the light and deliver it to a spectrometer (see Ref. (78) for more details). The angle-dependent reflectivity of a 4-pair hybrid cavity is shown in Fig.4-4a. Here we observe two dispersive dips in the reflectivity spectra that undergo anticrossing around the energy of the BODIPY-Br exciton (530nm).

These two features are identified as the lower (LPB) and upper polariton (UPB) branches, and we have used a two-level oscillator model to fit their dispersions (the solid lines in Fig.4-4a). It can be seen that the description of the measured data is excellent.

TMR model was used to extract the Rabi splitting energy for each of the different cavities and this is shown in Fig.4-4b together with experimentally measured data. We note that the Rabi splitting energy is primarily dependent on the number of absorbers per unit length in a cavity. However, here we attribute changes in the Rabi splitting to variations in the effective cavity length ( $L_{eff}$ ). As can be seen, we observe an increase in Rabi splitting energy as the number of DBR pairs on the bottom hybrid mirror is reduced, with the cavity incorporating a 1-pair hybrid DBR having a Rabi splitting energy that is around 14% larger than the DBR-DBR control. Evidently, as the number of DBR pairs in the hybrid mirror is reduced,  $L_{eff}$  is reduced which results in an effective “concentration” of the electromagnetic field into the active cavity region and an increase in the Rabi splitting. From Fig.4-5, where electric field simulations of the cavity mode for the 1-pair

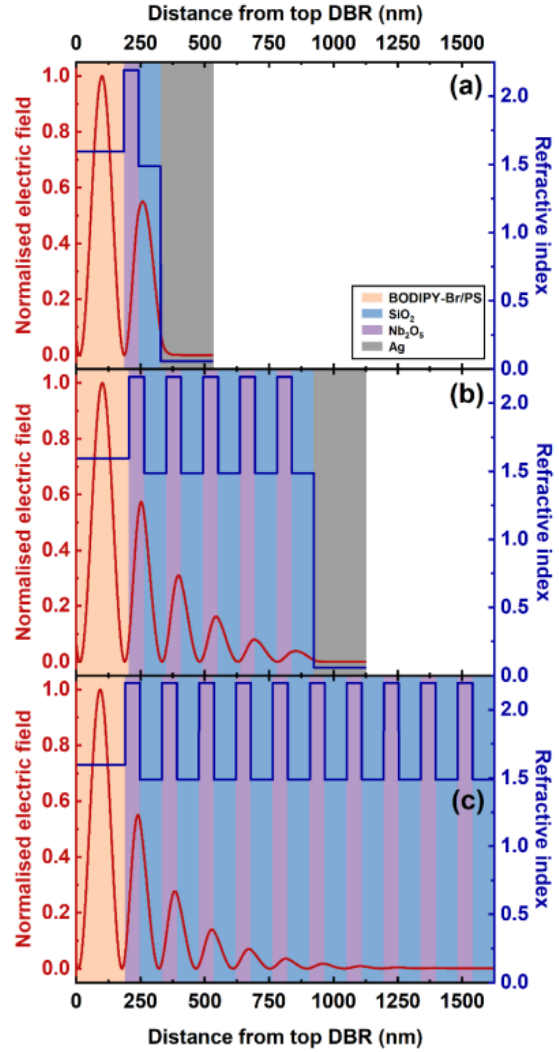


Figure 4-5: Electric field simulations of the cavity mode (red) and refractive index (blue) for (a) the 1-pair hybrid cavity, (b) the 5-pair hybrid cavity, and (c) the DBR-DBR control cavity. From this, it can be seen that the penetration length of the E-field changes in the different mirrors. Here, we omit the top DBR mirror as it is the same for all cavities, and thus the x-axis denotes the distance from the interface between the top DBR and the active layer. The different layers are shaded for clarity. Adapted from Reference (3).

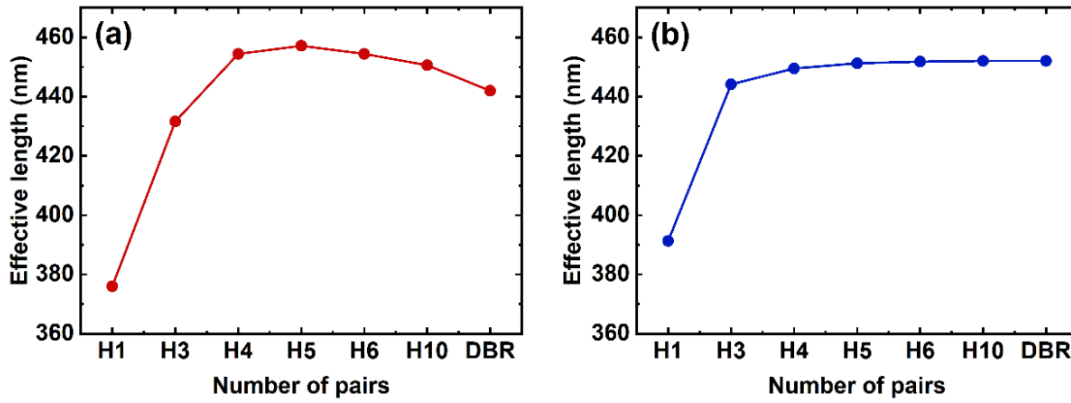


Figure 4-6: Effective lengths of the hybrid and DBR cavities. (a) shows the actual effective length, while (b) shows the effective length assuming a constant active layer thickness of 200 nm. From this it can be seen that the effective length increases as an increasing number of DBR pairs are added to the bottom mirror. Adapted from Reference (3).

and 5-pair hybrid cavities and the DBR control cavity are shown, it can be seen the penetration of the field into the different mirrors and the refractive index variation in each structure. This confirms the increased effective cavity length of structures incorporating an increased number of DBR pairs and it was calculated, Fig.4-6, using Ref.(79). However, for simplicity, in Fig.4-4b we show the penetration depth of the electromagnetic field into the bottom mirror only.

To explore the effect of the hybrid mirror on cavity Q-factor, we focused imaged a  $445\text{nm}$  pulsed laser beam into a  $4\mu\text{m}$  diameter spot on the cavity surface to generate PL emission. A k-space imaging setup was then used to collect the luminescence and image it into a CCD spectrometer, allowing the FWHM emission linewidth of the LPB at normal incidence to be determined. Figure 4-4c plots the normal incidence LPB linewidth measured from the various structures. It can be seen that there is an apparent reduction in LPB linewidth as the number of mirror pairs is increased, with this trend reversing for structures having more than 5 DBR pairs. However, this ‘reversal’ effect largely results from the fact that there was a small variation in the cavity mode wavelength caused by unintended variations in the thickness of the cavity active layer caused by the spin-coating process. This modifies the relative exciton–photon fraction of the LPB, with the photon fraction increasing (and linewidth reducing) as the negative detuning (energetic separation between

the photon mode and the exciton) increases. We can account for this effect in our model by using the known  $n$  and  $k$  data for the BODIPY-Br/PS film. This was input into a TMR model to describe the dispersion of the LPB and UPB for each cavity. From this, we were able to calculate the physical thickness of the organic film, the position of the cavity mode at normal incidence, and the LPB linewidth. This data is also plotted in Fig.4-4c, where we again find a good agreement between model and experimental results.

Using our model, we are then able to calculate expected cavity Q-factor as a function of the number of DBR mirror pairs. Here, we ‘turn-off’ the exciton oscillator strength and calculate the LPB linewidth and cavity Q-factor assuming in all cases the cavity mode is located at  $547\text{nm}$ . The results of our model are shown in Fig.4-4d. Here, we find the cavity Q-factor increases as the number of DBR pairs in the hybrid mirror is increased, and for 4 or more pairs, exceeds that of the DBR–DBR control. Furthermore, our model suggests that a cavity utilising a hybrid mirror consisting of 10 DBR pairs on top of an *Ag* film is expected to have a Q-factor that is 24% larger than an equivalent ‘conventional’ cavity whose bottom mirror does not contain *Ag*, (i.e. simply composed of a 10-pair DBR). As expected, we find that the measured and modelled polariton linewidths shown in Fig.4-4c are strongly dependent on mixing between the exciton and photon. For example, for the 1-pair hybrid cavity, we determine (by modelling and experiment) an LPB linewidth of around  $7\text{meV}$  at normal incidence. However, the Q-factor of the same cavity is  $\sim 1000$ , suggesting an uncoupled photon-linewidth of around  $2.2\text{meV}$ . This substantial broadening of the LPB linewidth occurs even though the excitonic fraction of this state is relatively small (being 13% exciton and 87% photon). As we discuss below, this broadened polariton linewidth masks a small amount of site-to-site variation of the cavity photon energy that occurs as a result of structural disorder within the cavity that only becomes apparent when polaritons undergo condensation and lasing.

## 4.4 Condensation in metal-DBR microcavities

We have explored our structures for evidence of polariton condensation. Here, it was decided to explore such effects in cavities that had the largest difference in their structural properties. Condensation effects were therefore studied in a 1-pair hybrid cavity and compared to a DBR–DBR control. In these experiments, the hybrid cavity utilised an 8-pair top DBR mirror. The DBR–DBR control structure was based on 10 and 8 DBR pairs, with the 10-pair mirror being fabricated by Helia Photonics Ltd. In both cases, the cavities had a very similar exciton–photon detuning, with the LPB being positioned at 567 and 569nm in the hybrid and DBR cavities, respectively.

A simplified setup schematics used in this experiment is shown on Fig.4-7. The setup operates at the reflection configuration, meaning the same objective 20x Mitutoyo Plan Apo, NA = 0.42) is used to pump the cavity and to collect the output emission from the cavity. To separate a pumping laser emission and polariton photoluminescence a Longpass Dichroic Mirror (DMLP) with razor edge at 490nm was used.

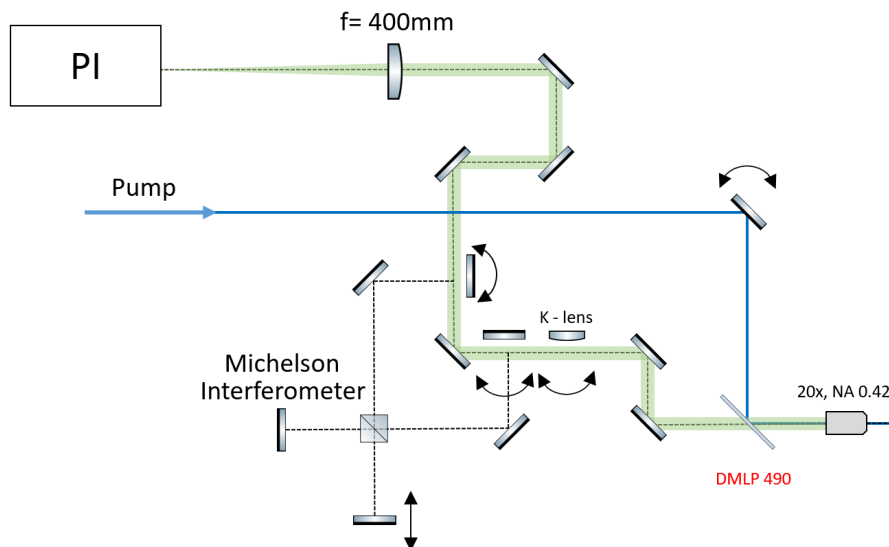


Figure 4-7: Schematic of the experimental setup in the reflection configuration. The setup allows for single-shot excitation and detection measurements of real-space and k-space spaces. It also enables single-shot interferometry measurements with tunable delay-stage to study either temporal or spatial coherence properties.

To generate polariton condensation, the microcavities were pumped non-resonantly

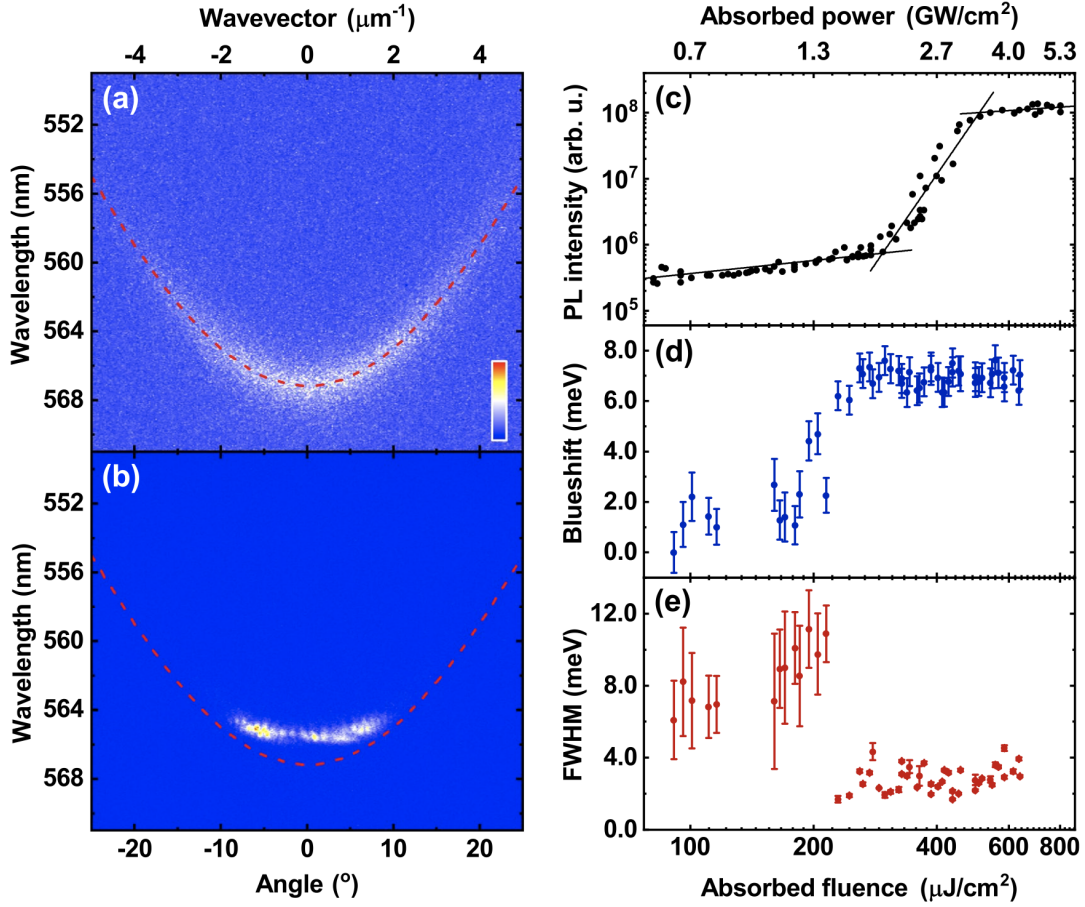


Figure 4-8: 1-pair hybrid mirror cavity condensation results. Normalised dispersions taken (a) below threshold and (b) above threshold. In both cases the red dashed line is a fit to the LPB in the linear regime. (c–e) Show the dependence of (c) PL intensity, (d) blueshift, and (e) full-width at half-maximum (FWHM) of the LPB on the absorbed pump fluence. From straight line fits to the power-dependent PL intensity in (c) (black solid lines), we determine a condensation threshold for this cavity of  $295 \mu\text{J}/\text{cm}^2$ . Here we see a non-linear increase in PL intensity, a spectral blueshift, and a decrease in the FWHM of the LPB. The error bars in (d) and (e) were calculated from the error on a Gaussian fit to the LPB at each fluence. Adapted from Reference (3).

at normal-incidence using a single-shot imaging technique in reflection configuration, with emission detected using k-space imaging. Here, the laser pulses (width of  $150\text{fs}$ , repetition frequency of  $15\text{Hz}$ ) were focused onto the cavity surface into a spot with a FWHM diameter of  $30\text{m}$ . For both cavities, the excitation laser wavelength was tuned to the first Bragg minimum at the edge of the stopband ( $467\text{nm}$  for the hybrid cavity and  $462\text{nm}$  in the DBR–DBR control) to maximise the transmission of light into the cavity. In the data presented below, the PL intensity for the power

dependence graphs was obtained by integrating single-shot real-space images of the cavity emission. The blueshift and FWHM data were extracted from the single-shot k-space dispersion images profiles filtered over  $\pm 0.075 \mu m^{-1}$  range around  $k = 0$ .

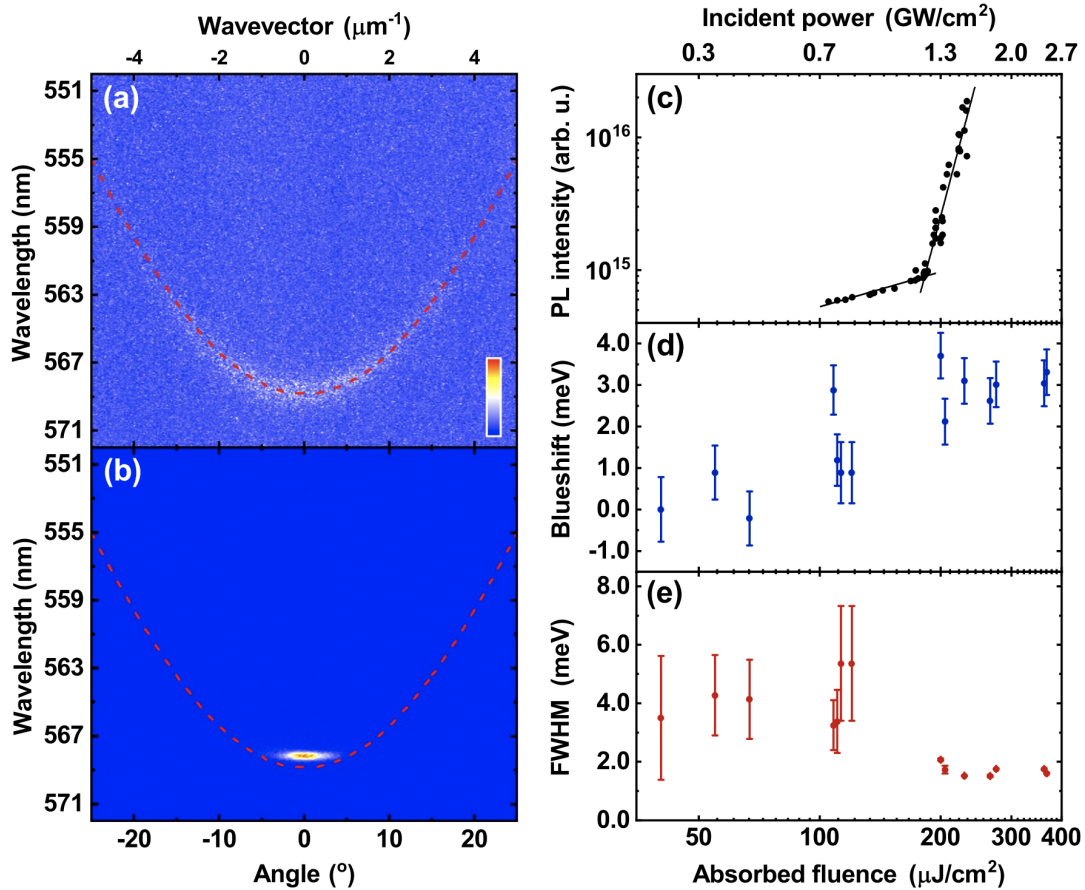


Figure 4-9: DBR-DBR control cavity condensation results. Normalised dispersions taken (a) below threshold and (b) above threshold. In both cases the red dashed line is a fit to the LPB in the linear regime. (c-e) Show the dependence of (c) PL intensity, (d) blueshift, and (e) full-width at half-maximum (FWHM) of the LPB on the absorbed pump fluence. From straight line fits to the power-dependent PL intensity in (c) (black solid lines), we determine a condensation threshold for this cavity of  $180 \mu J/cm^2$ . Here we see a non-linear increase in PL intensity, a spectral blueshift, and a decrease in the FWHM of the LPB. The error bars in (d) and (e) were calculated from the error on a Gaussian fit to the LPB at each fluence. Adapted from Reference (3).

Figure 4-8a plots the normalised PL emission from the hybrid mirror cavity recorded below the condensation threshold, together with a TMR model fit to the LPB dispersion. Here it can be seen that emission is initially distributed across a large angular range. We find that as the pump fluence is increased above the

condensation threshold, there is a non-linear increase in PL intensity (see Fig.4-8c), accompanied by an energy blueshift (Fig.4-8d) and a decrease in the linewidth (Fig.4-8e). Such blueshifts of the LPB have previously been explained on the basis of a partial saturation of the BODIPY optical transition (27). Figure 4-8b shows the normalised PL emission above threshold, with the fit to the LPB below threshold also shown, allowing the extent of the energy blueshift to be clearly seen. Specifically, we determine a condensation threshold (determined from the measured absorbed fluence) of  $295\mu J/cm^2$  which is accompanied by a blueshift of  $7meV$  and a reduction in LPB FWHM linewidth from  $11meV$  to  $\sim 2.8meV$ .

The equivalent condensation dataset to Fig.4-8 for the DBR-DBR control is shown in Fig.4-9. From part (c), we determine a condensation threshold of  $180\mu J/cm^2$ , which is accompanied by a blueshift of approximately 3 meV (part d) and a reduction in emission linewidth from  $5meV$  to  $\sim 1.6meV$  (part e). Interestingly, it is clear that the blueshift observed in the hybrid mirror cavity ( $7meV$ ) is more than twice that in the DBR cavity ( $3meV$ ). A larger blueshift is expected in the hybrid mirror cavity for a given reduction in molecular oscillator strength, an effect that we attribute to its enhanced Rabi splitting (39).

If we compare the distribution of emission in k-space for both cavities above threshold (Figs.4-8b and 4-9b), it is evident that in the DBR-DBR control, the emission is strongly concentrated around the bottom of the LPB. In contrast, we do not evidence a full collapse to  $k = 0$  in the hybrid mirror cavity; rather, the emission appears to be distributed over a wider range of k-vectors and energies and is apparently finely structured. We investigate the cause of this effect in "Investigating cavity homogeneity" below. Below threshold, the emission from both cavities is unstructured and has a size approximating the laser excitation spot ( $20\sim 30\mu m$  (FWHM)). Above threshold, the condensate in both types of cavity has a complex structure and consists of one or more separate domains having a size of between  $\sim 5$  and  $20\mu m$ . This effect has been previously observed and has been ascribed to interactions between the polariton condensate and the exciton reservoir (80; 58)

## 4.5 Cavity homogeneity

To explore the origin of the structure in the LPB dispersion above threshold, we used a spatial mapping technique to measure the PL emission from the LPB as a function of position for both the 1-pair hybrid cavity and the DBR–DBR control. Here, the sample was mounted on a motorised (x, y) stage that was incorporated into the k-space imaging setup, with sub-threshold emission mapped over an area of  $(26 \otimes 26)\mu\text{m}^2$  in step-sizes of  $1\mu\text{m}$  using a laser focused to a diameter of around  $4\mu\text{m}$ . From the PL spectra recorded, the peak emission energy at  $k = 0$  at each position was then determined across the cavity surface. We also calculated the range of peak emission energies across the cavity and their standard deviation (SD). To gauge the significance of our results, we also attempted to characterise the spectral resolution of the mapping system. Here, light from a Ne/Ar lamp was directed into the spectrometer with its entrance slit set to  $20\mu\text{m}$ , and it was found that the emission line at  $585\text{nm}$  had an apparent linewidth (FWHM) of  $0.68\text{meV}$ . Note, however, this measurement should only be viewed as an approximation of the true system resolution, as the k-space mapping setup required the entrance slit of the spectrometer to be fully-open in order to characterise the emission dispersion.

We first explored the emission from the DBR–DBR control cavity. A typical  $(25 \times 25)\mu\text{m}$  images are shown in Fig.4-10a,b. From Fig.4-10a it can be seen that there is a gradual transition in LPB energy across the image, indicating that there is a slight ‘wedge’ in the cavity optical path-length. This effect possibly results from a gradual variation in the thickness of the BODIPY-Br active layer. From an analysis of the two images collected, it was determined that the peak energy of the LPB is distributed over an energy range of around  $1.3\text{meV}$  with a standard deviation of  $0.29\text{meV}$ .

Using the same technique, we attempted to characterise the 1-pair hybrid cavity. Here, the cavity that was used had a slightly lower Q-factor than the cavity discussed in section 4.3 "Optical properties of hybrid microcavities" as a result of a reduced number (8) of DBR pairs in the top mirror. In this case, due to the relatively broad LPB linewidth ( $10\text{meV}$  at  $k = 0$ ) we were unable to resolve statistically significant

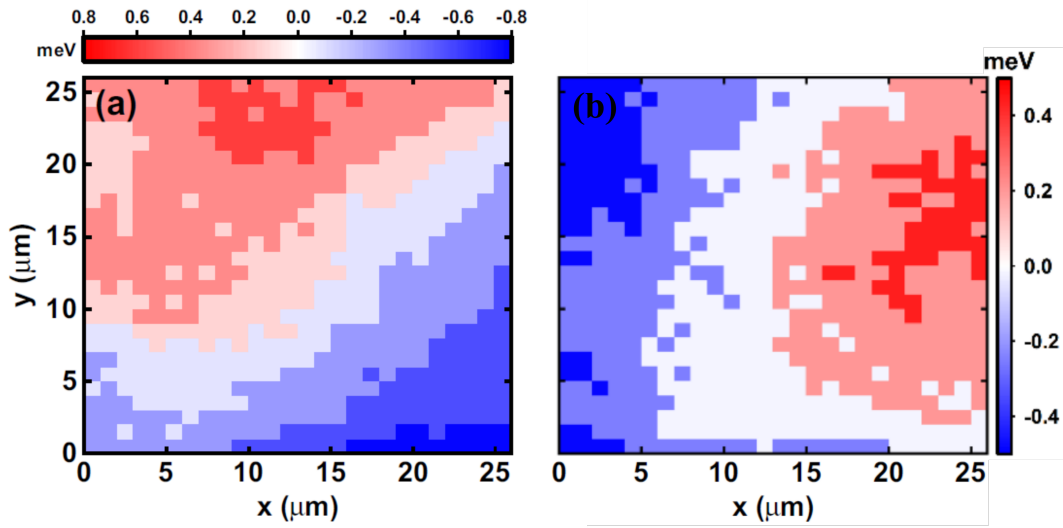


Figure 4-10: (a) Shows a sub-threshold polariton emission map of the variation in LPB emission energy from the DBR–DBR cavity from which condensation was observed. The colour scale corresponds to the variation of the LPB energy (in units of meV) around its average emission energy. (b) shows an additional PL map for the DBR-DBR control cavity. Adapted from Reference (3).

differences in LPB energy across the cavity surface.

Therefore, to further characterise cavity homogeneity, cross-sectional SEM images were recorded. Figure 4-11a,b show SEM images of the 4-pair hybrid and 10-pair DBR mirrors, respectively. Significantly, we find evidence for voids between the Ag and  $SiO_2$  layer in the hybrid mirror structure having a lateral length-scale of a few  $100nm$ , with resultant disorder apparently propagating into the DBR layers. In contrast, no such voids are evident in the DBR–DBR control, with the individual mirror layers having a high degree of uniformity. We speculate that such voids in the hybrid mirror cavity are highly likely to result in local fluctuations in effective cavity length. We have also used AFM to image the various layers that constitute the hybrid mirror and the DBR control and have used this to extract the root mean square roughness. It was found that both the Ag and  $SiO_2$  layers are individually very smooth; however, we detect enhanced roughness from both an Ag/ $SiO_2$  bilayer and the 1-pair hybrid mirror. Such layers are in fact rougher than the 10-pair DBR fabricated by Helia Photonics Ltd. We suspect the enhanced roughness of the 1-pair hybrid mirror results from poor adhesion between the Ag and  $SiO_2$  layers and results in the voids observed in Fig.4-11b.

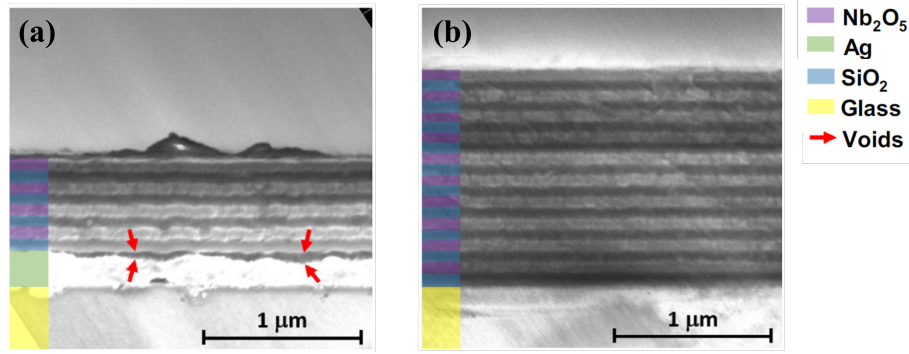


Figure 4-11: (a),(b) Show SEM images of the 4-pair hybrid and 10-pair DBR mirrors respectively. In (a), voids can be seen between the *Ag* and first *SiO*<sub>2</sub> layer Adapted from Reference (3).

## 4.6 Discussion

We have observed polariton condensation in a hybrid mirror cavity and in the DBR–DBR control at an absorbed fluence threshold of  $295\mu\text{J}/\text{cm}^2$  and  $180\mu\text{J}/\text{cm}^2$ , respectively. It appears that the ratio of condensation thresholds scales inversely with cavity Q-factor, with the DBR–DBR cavity undergoing condensation at a threshold that is 1.6 times lower than that of the hybrid mirror cavity and possessing a cavity Q-factor that is 1.7 times greater (1190 and 710, respectively). We note that the condensation threshold of  $180\mu\text{J}/\text{cm}^2$  in the DBR–DBR control observed here is slightly lower than that observed in previous studies on a similar microcavity containing BODIPY-Br which was determined as  $530\mu\text{J}/\text{cm}^2$ <sup>18</sup>. We suspect such differences may result from the shorter pump-laser pulse-lengths used here ( $150\text{fs}$  compared to  $2\text{ps}$  pulses used in previous experiments), with reductions in lasing threshold being previously observed in weakly-coupled organic microcavities excited using shorter pump-pulses (81).

We now discuss polariton relaxation processes in the two types of cavities explored. It is clear that the mapping experiments described in section 4.5 "Cavity homogeneity" evidence a slowly changing energy landscape in the DBR–DBR cavity, with the lateral size of the polariton condensate being either similar to, or smaller than the length-scales over which the cavity path-length fluctuates. Specifically, we find that the energy of the LPB changes by around  $0.6\text{meV}$  over distances of around  $10\sim 20\mu\text{m}$  (the typical condensate size). This level of dis- order is smaller than the

linewidth of the condensate emission ( $1.6\text{meV}$  at  $k = 0$ ), and thus the ‘energetically flat’ landscape of this cavity allows complete relaxation to the ground polariton state.

In the hybrid mirror cavity, however, we find that condensate emission does not undergo complete collapse to  $k = 0$ , but is finely structured and distributed over a wider range of  $k$ -vectors. In these cavities, SEM images evidence spatial disorder at the interface between the DBR and the silver mirror having a lateral length-scale of a few  $100\text{nm}$ , with this disorder propagating through the DBR. At present, the relatively large linewidth ( $10\text{meV}$ ) of the LPB below the condensation threshold (which is mainly broadened by exciton–photon mixing) effectively masks energetic disorder within the cavity. Once the condensation threshold is reached, however, the narrowed condensate emission linewidth now allows energetic disorder within the cavity to be evidenced through the fine-structure that emerges in the emission dispersion curve (see Fig.4-8b). This structure indicates that the ‘fragmented’ condensates that are formed exist in a relatively disordered landscape resulting from local variations in the cavity path-length, with the condensate linewidth ( $2.8\text{meV}$  at  $k = 0$ ) being almost a factor of two greater than that observed in the DBR–DBR control cavity. We note that similar structure in  $k$ -space emission has previously been observed in GaN and MeLPPP microcavities and has also been attributed to thickness variations in the active layers (82; 83).

We suspect that the increased structural disorder in the hybrid mirror cavity results from poor adhesion between the  $Ag$  and  $SiO_2$  layers, which results in a series of voids at this interface. We have made preliminary attempts to reduce this issue; for example, we have determined that the surface roughness of an  $Ag/SiO_2$  bilayer is not dependent on the deposition rate of  $SiO_2$ . It is possible that other techniques could be used to improve the quality of the interface between these layers—for example, using adhesion promoters or thermal annealing during deposition to encourage the  $SiO_2$  to better adhere to the  $Ag$  film. Conversely, it may be possible to construct ‘upside-down’ hybrid mirror cavities, with the  $Ag$  layer deposited onto the final top surface of the cavity. This approach might result in an improved interface between the  $SiO_2$  and  $Ag$  layers; however, such cavities would likely require optical

measurements to be made through the bottom glass substrate. While this would not be an issue for linear optical spectroscopy, such a geometry is not well suited to transient measurements due to multiple internal reflections within the thick glass substrate.

"If your experiment needs statistics,  
you ought to have done a better ex-  
periment."

Ernest Rutherford

## Chapter 5

# Photon statistics of organic polariton condensates

### 5.1 Overview and motivation

In this chapter I develop an alternative approach to access second-order coherence which is based on well-controlled single-shot detection allowing for direct measurements of photon statistics of polariton condensates. Similar approaches relying on single photodetector measurements have been used previously to study second-order coherence in atomic condensates (84; 85). Using this technique I demonstrate an unexpectedly low excessive quantum noise of around 1.9% for spatially highly fragmented organic polariton BECs at room temperature. Reducing the size of the system increases the condensation threshold, nonlinearities, and effective polariton thermalization rate due to kinetic losses originated from ballistic propagation of polaritons out of the condensate area (86). However, it does not reduce the degree of fragmentation in a condensate, which has been discussed in recent reports (87; 88), but instead enhance shot-to-shot fluctuations.

Macroscopic quantum phenomena in polariton systems has been the subject of an extensive research going far beyond purely fundamental interest (26; 89; 90; 91). Much attention has been paid to understand the coherent nature of organic polariton condensates and its relation to onsite nonlinearities (39; 27) as well as disorder (80; 88). Long-range order and temporal coherence of polariton condensates at room

temperature have been shown by means of Michelson interferometry and via line-narrowing in spectroscopic measurements (92; 24; 35; 39; 43). Although first-order coherence is essential to manifest BEC formation, in principle, it cannot discriminate between coherent and thermal states due to the lack of quantum statistical information of light.

Quantum statistics of weakly interacting BECs of ultra-cold atoms resembles Poisson distribution like an ideal laser (85). In this respect polariton BECs can be very different from the atomic ones (93; 94). High thermal fluctuations (95), onsite nonlinearities (96; 5; 97), and condensate depletion (98; 99) as well as mode competition (100) can significantly broaden particle number distribution thereby increasing quantum fluctuations way above the shot-noise limit. Quantum statistics of solid-state BECs besides the fundamental importance have a certain connection to applications. In a similar way the laser shot noise defines limits for laser cooling (101), precise interferometry (102) and others, noise in polariton condensates sets boundaries for emerging polariton applications (103; 26; 104; 105; 106; 107; 108; 109; 110; 111; 100). In a recent report on single-photon switching, Zasedatelev et al. (112) underpins the role of shot-to-shot intensity fluctuations of the condensate that compromise switching fidelity. Thus, understanding the quantum statistics is crucial in view of novel devices.

Until now, second-order coherence and photon statistics of room-temperature polariton condensates remain an unexplored territory. From a theoretical point of view polariton BECs are complex open dissipative systems which intrinsically are far from equilibrium (113). Moreover, unlike polariton BECs at cryogenic environment, room temperature systems are also subject to high thermal fluctuations and strong spatial disorder inherent to most of the practical structures (80), rendering them extremely challenging for a theoretical study. On the experimental side the main problem is sub-picosecond polariton dynamics that cannot be acquired in standard Hanbury Brown and Twiss (HBT) measurements due to the insufficient time resolution of single-photon avalanche photo detectors of  $\sim 40$  ps (114). Advanced techniques for high-order correlation measurements based on photon counting with a streak camera (115; 116) enable more than an order of magnitude improvement

in time resolution but are still limited to few picoseconds (117) and usually, in case of inorganic microcavities, require high repetition rates  $\sim 10^8$ Hz to collect enough photon statistics. Even though organic polariton emission is more intense and the repetition rate can be diminished, intrinsic photobleaching of organic microcavities does not allow them to tolerate more than roughly several million pulses (118; 112).

In this regard, second-order coherence properties of a polariton condensate and intensity statistics of an integrated polariton photoluminescence are thoroughly analyzed, with respect to pumping power, pump spot size, and data windowing. Let us now firstly discuss an experimental setup and techniques used to conduct this study.

## 5.2 Experimental setup design

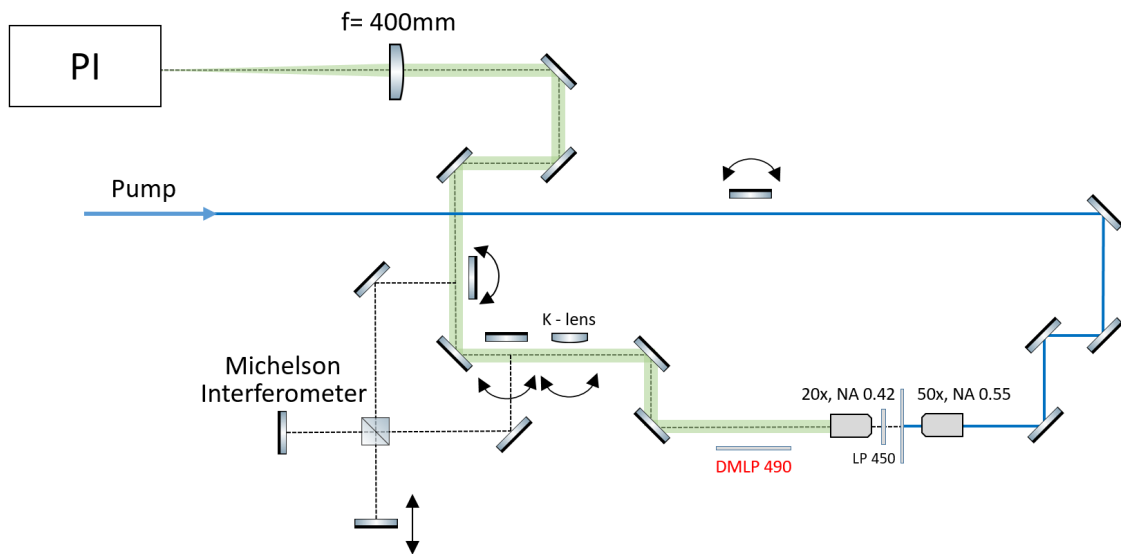


Figure 5-1: Experimental setup that allows for single-shot excitation and detection measurements of real-space and k-space images in transmission configuration. It also enables single-shot interferometry measurements with tunable delay-stage to study either temporal or spatial coherence properties.

In this section, to begin with, I describe the design of the experimental setup, set of equipment used throughout this part of work, and different configurations this setup can operate at with an experiment schematic shown on Fig.5-1. The heart of the setup is a high energy Ti:Sapphire regenerative amplifier (Coherent

Libra-HE) that generates 800nm pulsed emission at a varying repetition rate from 10Hz to 1000Hz with a varying temporal width of the pulses from  $\sim 100$  fs to  $\sim 2$  ps. here pulses of  $\sim 2$  ps are used in order to reduce pulses' peak energy which in turn prevents unwanted and inevitable photodegradation of a polymer and allows for a broader range of excitation fluences in threshold units. Laser pulses then were focused on a BBO crystal to generate second harmonic emission at 400nm which consequently is focused on a sample by a focusing objective (50x Mitutoyo Plan Apo, NA = 0.55). A focusing objective is placed on a translational stage that allows one to adjust the size of the focusing beam in a sample plane. To collect the output emission from the sample in transmission configuration another objective (20x Mitutoyo Plan Apo, NA = 0.42) is used. Photoluminescence is then coupled to a Princeton Instruments SP2750 spectrometer with an EMCCD camera Princeton Instruments ProEM 1024BX3. The emission can be detected either in a real space or reciprocal momentum space by putting an additional 1000mm conjugated lens (k-lens) to project the Fourier plane of the collecting objective to the slit. Replacing mirror with a 1200 grooves/mm grating allows one to spectrally resolve resulting emission that goes through a spectrometer entrance slit of  $200\mu m$  width. To cut the residual 400nm emission that inevitably goes through the cavity an additional long-pass (LP) edge filter at 450nm was placed between the collecting objective and the sample. An additional option to study first order coherent properties of the emission both temporal and spacial is realized by using adjacent Michelson interferometer, that one can switch to by using a flip mirror to redirect a polariton PL.

To calibrate the incident excitation fluence of the pump pulse, the average pump power is measured using a calibrated Si photodetector Thorlabs-Det10/M and an oscilloscope Keysight DSOX3054T

With this being described, we can now discuss the cavity design and other details of the experiment in the next chapter.

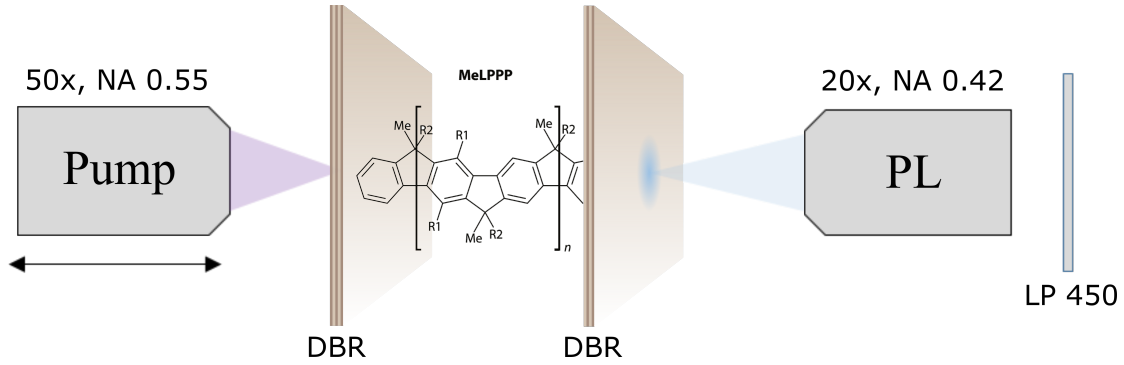


Figure 5-2: A transmission detection configuration technique with a schematic cavity design under study. A pumping objective positioned on a translational stage is used to create Gaussian pumping pulses of a varying spatial size. Long-pass (LP) edge filter is used to block residual pumping laser emission.

### 5.3 Cavity design

Here a methyl-substituted ladder-type poly(paraphenylene) (MeLPPP) is utilized, for realizing polariton physics (112; 26; 92; 119), Fig.5-2. The cavity design consists of a thin 35-nm film of MeLPPP placed between two 50-nm spacers of  $SiO_2$ , which in turn are sandwiched between two  $SiO_2/Ta_2O_5$  distributed Bragg reflectors (DBR) on a glass substrate. This  $\lambda/2$  organic microcavity exhibits an energy splitting of 150meV between the exciton resonance (2.72eV, 2.91eV) and the lower polariton branch (2.582eV) (Rabi-splitting), which is of the detuning order between bare cavity and the exciton modes, fixed across all sets of measurements in this work (140meV, LPB/exciton). In particular, Hopfield coefficients, or exciton and cavity photon fractions, for the lower polariton state are the following:  $|X|^2 = (1 + \delta/\sqrt{(\delta^2 + \Omega^2)})/2 = 0.162$  and  $|C|^2 = (1 - \delta/\sqrt{(\delta^2 + \Omega^2)})/2 = 0.838$ .

### 5.4 Second-order coherence

Under a non-resonant 2ps pulsed excitation at 400nm and 10Hz repetition rate focused down to  $44\mu m$  spot size, 300 successive single exciton-polariton realizations are measured. To exclude the lab noise and laser drifts we postselect only those realizations that correspond to  $\pm 1\%$  range of the input pump pulse energy which has been set to  $2.1x$  the condensation threshold ( $2.1P_{th}$ ). As a result, we observe

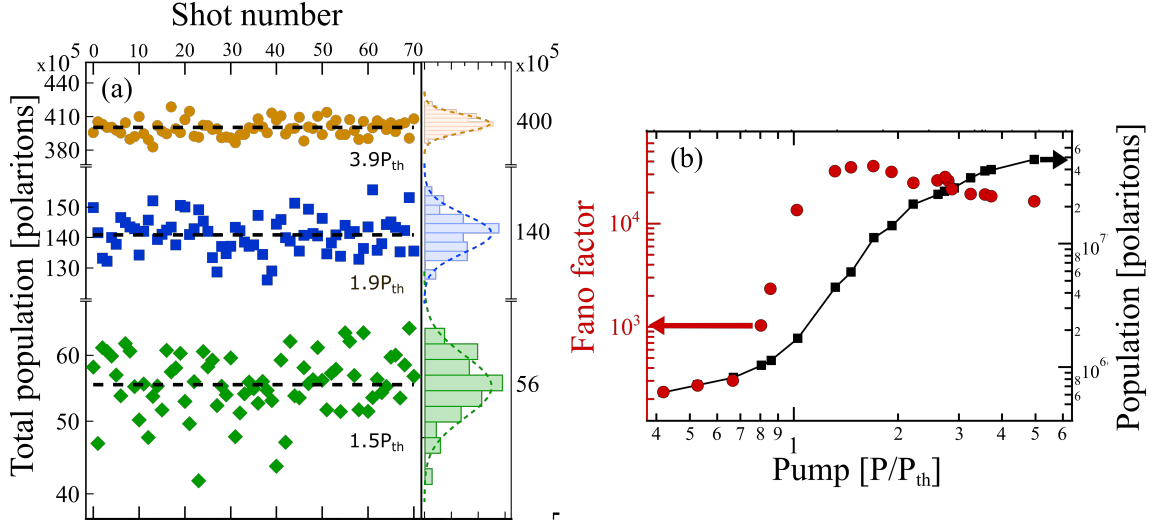


Figure 5-3: (a) Fluctuations of a total polariton number in a condensate at three different excitation pump fluences:  $1.5P_{th}$ ,  $1.9P_{th}$ , and  $3.9P_{th}$ , plotted with green, blue, and orange markers, correspondingly, for a spot-size with a FWHM of  $44\mu m$ . Right panel of figure (a) shows corresponding histograms of shot-to-shot particle number fluctuations (photon statistics). (b) Dependence of the Fano factor (red) and average polariton population (black) as a function of excitation fluency. Green, blue, and yellow dots correspond to distributions from panel (a).

fluctuations of the total polariton population in a condensate of up to 10 percent from the average value from realization-to-realization at a fixed excitation fluence ( $\pm 1\%$ ) Fig5-3a. Increasing the pump fluence leads to an increase of the average polariton population in a condensate according to the pump-power dependence Fig5-3b (right axis) and simultaneously to the narrowing of the polariton population distribution Fig5-3a (different colours).

To quantify shot noise in the system we introduce the Fano factor,  $F = \sigma_n^2 / \bar{n}$ , that shows the deviation from pure Poisson statistics with  $F = 1$ . Fig5-3b demonstrates a rapid increase of noise in our system near the condensation threshold followed by a slight decrease the author introduces a time averaged zero-time-delay second-order particle correlation function:

$$\overline{g^{(2)}(0)} = 1 + \frac{\sigma_n^2 - \bar{n}}{\bar{n}^2} \quad (5.1)$$

where  $\bar{n}$  is the ensemble averaged number of polaritons in a condensate, or total population, and  $\sigma_n^2$  is the variance of this number. Time averaging results from the

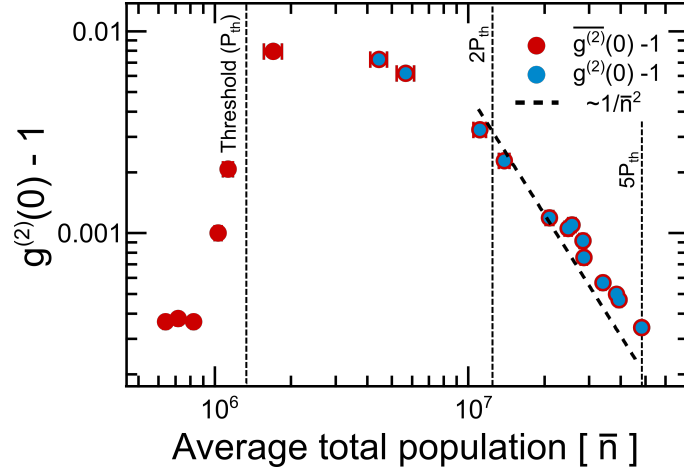


Figure 5-4: Zero-time-delay second-order correlation function of the polariton condensate as a function of total polariton population. Red dots represent measured  $(\overline{g^{(2)}(0)} - 1)$  time-averaged values calculated from experimental data shown in Fig5-3b. Blue dots correspond to the theoretical expectation of second-order correlation function values extracted from the fit of experimental data. Vertical black dashed lines show the total polariton population at the condensation threshold, 2 times the condensation threshold, and 5 times the condensation threshold, respectively. The black dashed line represents a model fit of experimental data with a  $\sim 1/\bar{n}^2$  function.

fact that even though we deal with pulsed-driven polariton condensates and operate in a single shot detection regime, we still integrate all the emission over the condensate duration which is strongly dependent on the excitation duration time. For the current pumping conditions with 2ps pump pulses our recently developed microscopic model for an equivalent system (112) implies the lifetime of the condensate to be  $\sim 1ps$ . Moreover, the value of the average second-order coherence depends on the intensity correlation time. Applying the analysis described in reference (120), we extract the intensity correlation time of  $\approx 2.6ns$ . Therefore, the condensation lifetime limits the coherence in the system and the second-order coherence function being integrated over the condensate lifetime provides values asymptotically close to the theoretical expectation of  $g^{(2)}(0)$  values. This renders such approach to measure zero-time delay second-order coherence a powerful tool to probe photon statistics of polariton condensates at room temperature.

Since for coherent light-matter waves  $g^{(2)}(0,0) \equiv g^{(2)}(0) = 1$  and for strongly fluctuating condensates  $g^{(2)}(0) > 1$ , we observe a rapid transition of the system from a thermal to a coherent state as we do the power scan from 0.5 to  $5P_{th}$  Fig5-3b,

reaching a quite noiseless, second-order coherent condensation regime with a record  $g^{(2)}(0) = 1.00034$  at  $5P_{th}$ , implying that the intrinsic particle number fluctuation of a coherent state is around 100 times above the shot-noise limit Fig5-4. This regime is reached at gain saturation, as one can see from the pump-power intensity dependence of the photoluminescence emission in Fig5-3b (right axis). Taking into account that we deal with  $\sim 10^7$  polaritons in the system, we can neglect the term  $1/\bar{n}$  in equation 5.1, and hence, Fig5-4 essentially shows the dependence of  $\sigma_n^2/\bar{n}^2$  on  $\bar{n}$ . Since we observe a good agreement with a fit function  $\sim 1/\bar{n}^2$ , we can conclude  $\sigma_n^2$  is a weakly growing function of an average total population  $\bar{n}$ , while in the classical case the noise is defined by fluctuations of an average photon number  $n$ , and  $\sigma_n^2 \sim n^2$  (121). Therefore, from Fig5-4 we can infer that the noise in our system does not have the classical origin, but manifests thermal and quantum nature of BECs with a complex interplay that can be witnessed by the width of photon number distributions depicted in Fig5-3a. This result is rather surprising accounting for the large dynamical instability and disorder inherent to organic systems when studied in the single-shot excitation regime.

Instability and disorder have been the subject in several recent works which experimentally studied the origins of spacial filamentation, or fragmentation, of polariton condensates (87; 88; 80). In-depth investigation of condensate filamentation under single-shot excitation in high-Q GaAs-based microcavities was attributed to effective self-focusing, or hole-burning, which caused the appearance of a prevailing contribution of the effective attractive interaction over the repulsive mean-field one for highly photonic polaritons (87). This effect is possible in the regime of short-pulse excitation allowing for complete depletion of the exciton reservoir within a single realization of the condensate, however, it is unlikely the case in our system, as we deal with 2ps pulsed excitation and  $\approx 280$ fs polariton lifetime, that, once above condensation threshold, works as a quasi-stationary excitation that continuously replenishes and effectively clamps the exciton reservoir accordingly under stimulated depletion towards the condensate. For the organic systems, the role of disorder on condensate fragmentation was firstly discussed by Daskalkis et al. (80). Work by Bobrovska et al. (88) experimentally demonstrated a dynamical instability of con-

condensates leading to the formation of multiple spacial domains and depending on the size of spatial pump profiles.

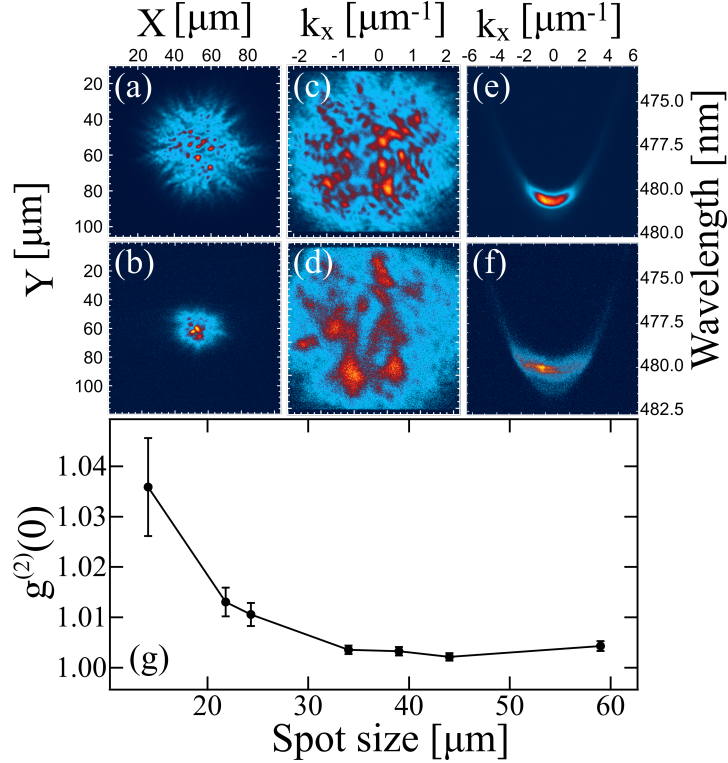


Figure 5-5: (a),(b) Real-space images of single condensate realizations obtained at two thresholds for two different excitation spot sizes: 44 μm and 13 μm at FWHM, respectively. (c),(d) Corresponding single shot images in momentum space obtained at the same excitation conditions, and (e), (f) integrated over 500 single-shot realizations dispersion images. (g) Second-order coherence function at zero time-delay as a function of excitation spot size.

## 5.5 Spot-size analysis

To reduce the degree of fragmentation and to explore the behaviour of the quantum noise in the condensate, we vary the pump size of the Gaussian beam in the range between 13 and 59 μm, and extract the  $g^{(2)}(0)$  values for 7 different spot sizes under the same pumping conditions. To exclude any bias from sample inhomogeneity, each spot-size value aggregates 8 different positions on the sample with 300 successive realizations collected. To minimize fluctuations of the condensate occupancy due to pump induced exciton reservoir density variations and to avoid photodegradation at small spot sizes, we fix the excitation pump fluence at  $2P_{th} \pm 1\%$ . Fig5-5a,b shows

real-space images of single condensate realizations formed by 44  $\mu\text{m}$  and 13  $\mu\text{m}$  pump spots, respectively. Corresponding k-space images obtained at the same pumping conditions are presented in Fig5-5c,d. The experiment shows that instability is equally present regardless of the size of the condensates. Importantly, we observe a broadening of the polariton distribution in the momentum space by decreasing the spot size Fig5-5e,f evidencing an increase of the average group velocity of polaritons i.e., the tendency to occupy higher-momentum states due to more kinetic energy to outflow from the condensation area within the lifetime. At the same time we observe a substantial growth in the shot-noise of the condensate with decreasing the spot size Fig5-5g.

The expansion in momentum space is accompanied by an increase of the condensation threshold for small spot sizes. This leads to the hypothesis that kinetic losses of polaritons from the condensate due to polariton outflow are larger for smaller sizes and hence, a higher density of excitons is needed to reach the threshold. We consider the threshold pump fluence  $P_{\text{th}}$  to be proportional to the total losses  $\gamma$  from the LPB:

$$P_{\text{th}} \propto \gamma \quad (5.2)$$

There are two major channels in the energy dissipation rate of polaritons: the internal radiative losses that correspond to the photon leakage from the cavity,  $\gamma_0$ , and the external ones that occur due to the outflow of polaritons from the pumped area,  $\gamma_{\text{out}}$ , which can be estimated as follows:

$$\gamma_{\text{out}} = \frac{\langle v_{\text{gr}} \rangle L}{S} \quad (5.3)$$

where  $\langle v_{\text{gr}} \rangle$  – is the average group velocity of the polaritons, leaking from the pumped spot,  $L$  – is the circumference of the pumped area,  $S$  – is the area of the spot. Assuming that the excited area is a circle of diameter  $d$  and  $\gamma = \gamma_0 + \gamma_{\text{out}}$ , we obtain the following dependence for the threshold excitation fluence:

$$P_{\text{th}}(d) = P_{\text{th}}(\infty) \left( 1 + \frac{4\langle v_{\text{gr}} \rangle(d)}{\gamma_0 d} \right) \quad (5.4)$$

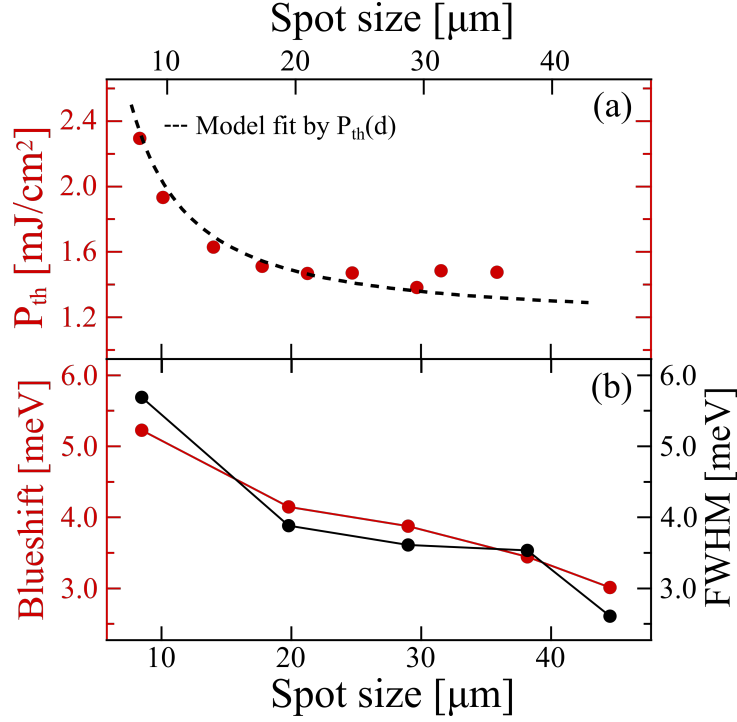


Figure 5-6: (a) Condensation threshold as a function of excitation spot size. (b) Blueshift and linewidth at FWHM of the condensate as a function of excitation spot size. The data have been obtained by averaging over 30  $E, k$  distributions of single condensate realizations for each spot size.

where  $P_{th}(\infty)$  is the threshold pump fluence in the limit of large spot size ( $d \gg \gamma_0/\langle v_{gr} \rangle$ ).

From an integrated dispersion image of a polariton condensate with a particular size (Fig.5-7a), we extract dependencies of the polariton occupancy,  $n(k) = N(k)/N_{tot}$  (Fig.5-7c), and polariton group velocities,  $v_{gr}(k) = dE(k)/dk$  (Fig.5-7d), on polariton wave vector  $k$  [ $\mu m^{-1}$ ], and calculate weighted average group velocity of polaritons in a designated radial direction from the center:

$$\langle v_{gr} \rangle = \sum_k n(k) V_{gr}(k) \quad (5.5)$$

Then, we repeat this procedure varying the size of the condensate from 20 to 55  $\mu m$  to find the dependence of weighted average group velocity on the system size,  $d$ , and fit this dependence with a function  $F = A + Bd^{-1}$ , Fig.5-8a, which we use to find the threshold constant in the expression for the dependence of condensate threshold on the system size Fig.5-8b:

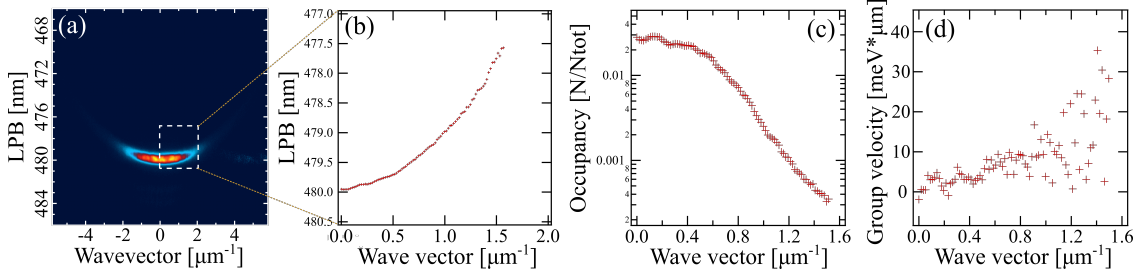


Figure 5-7: (a) Polariton dispersion at  $2P_{th}$  averaged over 500 realizations, (b) Fit of the polariton dispersion within condensation region by extracting LPB positions from k-vector cross sections of the dispersion image. (c) Dependence of polariton occupancy on a wave vector ( $n(k)$ ) where  $\int n(k)dk = 1$ . (d) Polariton group velocity dependence on wave vector.

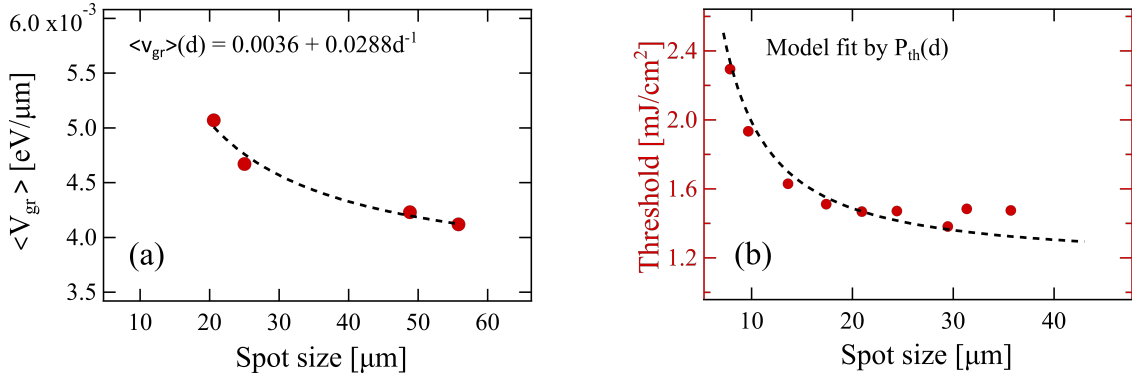


Figure 5-8: (a) Dependence of average weighted group velocity for condensate polaritons on the system size (red dots) and its fit with  $\sim d^{-1}$  function. (b) Dependence of threshold pumping density on system size and its fit with  $P_{th}(d)$  function.

$$P_{th}(d) = P_{th}(\infty) \left( 1 + \frac{4\langle v_{gr} \rangle^{fit}(d)}{\gamma_0 d} \right) \quad (5.6)$$

From dispersion imaging below threshold, we extract internal radiative losses  $\gamma_0 = 3.7 \cdot 10^{-3}$  (eV). From dispersion images at above threshold we extract the dependence of average group velocity of polaritons on the excitation spot size,  $\langle v_{gr} \rangle(d)$ , which increases with decreasing spot size. Using formula (5.4) we fit the experimentally obtained threshold fluence values (Fig.5-6a, red axis). The following values corresponds to the best fit result and experiment, respectively:

$$\begin{aligned} P_{th}(\infty) &\approx 1.2 \text{ [mJ/cm}^2\text{]} \\ P_{th}^{exp}(\infty) &\approx 1.5 \text{ [mJ/cm}^2\text{]} \end{aligned} \quad (5.7)$$

The experiment shows that the condensation threshold reaches a plateau of  $\approx 1.5$  [ $mJ/cm^2$ ] above a certain spot size. We observe a nice quantitative agreement within  $\approx 25\%$  deviation from the best fit result of a threshold constant. One should keep in mind that our model is linear and lacking in taking into account nonlinearities that play a significant role in the polariton condensate dynamics (24; 39; 27). Therefore, further improvements of this model should include these effects.

Moreover, a non-linear threshold behaviour is accompanied by an tangible increase of the condensate blueshift. Fixing the pump fluence at around  $2P_{th}$  we do a single-shot dispersion imaging for 5 different spot sizes. Averaging dispersion images over 40 realizations at each spot size, we observe an increasing blueshift with decreasing the spot size Fig5-6b (red axis). This effect is accompanied by the broadening of the condensate linewidth of the spectra integrated over  $\pm 5\mu m^{-1}$  Fig5-6b (black axis). The build up of coherence in a condensate is affected by many parameters of the system, such as intrinsic nonlinearity (122), lifetime of exciton reservoir (123), presence of dark excitons (124), and characteristic times of relaxation processes (125). In our experiment this is rather limited by the dynamical blueshift that smears out the linewidth within the pump pulse duration and the condensate life-time.

To make sure that this effect has a physical nature rather than being a feature of analysis or measured instrumental noises, we examine how calculated  $g^{(2)}(0)$  values depend on the region of interest (ROI) of an integrated area of single-shot EMCCD images for all available sets of condensate images for different spot-sizes. We apply a circular mask with the diameter varying from  $1\mu m$  to  $100\mu m$  to real-space images of single condensate realizations, top insets on Fig5-9, and calculate  $g^{(2)}(0)$  values for each of the mask diameter, bottom left inset on Fig5-9. We observe that upon increasing the diameter of the mask in real-space, contribution of stochastic disorder to  $g^{(2)}(0)$  decreases, and starting from  $\approx 30\mu m$  ROI diameter condensates of all sizes reach their plateaus showing this remarkable increase in second order coherence function at zero-time delay once the condensate size is reduced. Decline of the black curve on the bottom left inset of Fig5-9 might be due to increased contribution of camera noise to integral intensity of the image, that keeps getting reduced upon

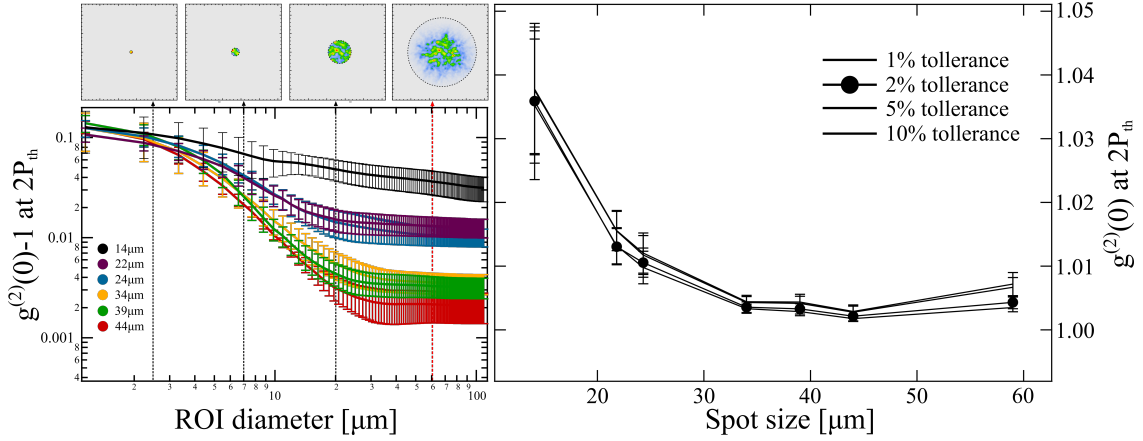


Figure 5-9: Bottom left figure shows dependencies of the calculated  $g^{(2)}(0) - 1$  values at zero time-delay at  $\sim 2P_{th}$  as a function of Region of Interest (ROI) size within which the real-space polariton intensity is integrated for different spot-sizes of the condensate:  $14\mu m$ ,  $22\mu m$ ,  $24\mu m$ ,  $34\mu m$ ,  $39\mu m$ , and  $44\mu m$ . Each point of each curve is averaged over 8 different positions on the sample, and error bars represent the spread. Right figure demonstrates dependence of the second-order coherence function at zero time-delay at  $\sim 2P_{th}$  as a function of an excitation spot size corresponding to cross section values along red dashed line from left panel. Top insets visualize ROI masks applied to real-space profile of a  $44\mu m$  condensate.

increasing the diameter of the mask. It is worth mentioning that since prior to the analysis of second-order coherence function we postselected only those realizations that corresponded to  $\pm 1\%$  range of the input pump pulse energy, changing this tolerance interval from  $\pm 1\%$  to  $\pm 2\%$ ,  $\pm 5\%$ , and  $\pm 10\%$  does not qualitatively affect noise properties of the system and does not change dependence, right inset on Fig5-9.

## 5.6 Integral emission properties

To understand the change in photon statistics with decreasing the size of the condensate (Fig5-5g) we need a detailed picture of the mechanisms behind polariton condensation at room temperature. Therefore, we explore its behaviour by reconstructing the experimental s-curves (pump-power dependencies) of a polariton emission with a recently developed multimode microscopic model (112) which describes the full dynamics of the system (for details see Section 5.7 "Microscopic Model"). One of the dominant relaxation processes within the lower polariton branch is the thermalization mechanism (92; 112) which was utilized to explain effective stimulated

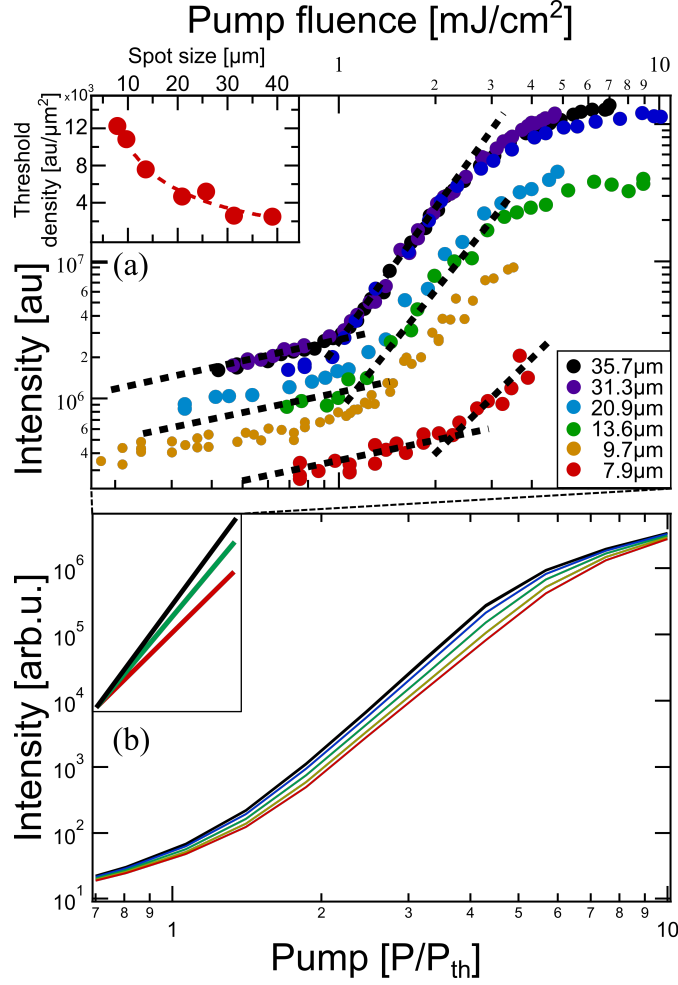


Figure 5-10: Dependencies of polariton photoluminescence on pump fluence for 6 different dimensions of a Gaussian pump profile with FWHM values from  $7.9$  to  $35.7\mu\text{m}$ . (a) Experimentally obtained s-curves (color dots) with fits of linear and non-linear parts of s-curve for small, medium, and large spot sizes (black dashed lines). (b) Model s-curves indicating slight change of  $\beta$ -factor for 6 different values of polariton losses,  $\gamma_{\text{out}} = \gamma_0 + \frac{\langle v_{\text{gr}} \rangle L}{S}$ , which correspond to 6 pump spot dimensions. Inset shows corresponding fits of nonlinear regions from experimental s-curves for small, medium, and large spot sizes, demonstrating slope change.

relaxation of polaritons towards the ground polariton state (113). The thermalization term in the rate equations appears in a form  $V_{\text{therm}}^{\text{eff}} \sim n_i(n_0 + 1)\gamma_{\text{low}}^{\omega_i, \omega_0}$ , where  $n_i$  and  $n_0$  are polariton densities at  $i$  and 0 (ground) energy states, and  $\gamma_{\text{low}}^{\omega_i, \omega_0}$  is a thermalization rate from higher energetic polariton states  $\hbar\omega_i$  towards the ground state  $\hbar\omega_0$  (112). This term evolves throughout the life-time of the polariton system demonstrating nontrivial dynamics. The increase in total loss at LPB leads to growth of the polariton population density below condensation threshold, the inset

of Fig5-10b shows the total polariton population density at the threshold. Therefore, the total thermalization in the systems is getting faster for smaller spot sizes. But with the further buildup of the condensate the increased total loss within LPB compromises accumulation of polariton density and thus, decreases the thermalization term above condensation threshold (for details see Section 5.8 "Numerical simulations"). Overall, it leads to an extension of the transient region at the cross-over from a thermal to a coherent polariton state, which is evident as a flattening of s-curves with decreasing the spot size, Fig5-10b. Thus, our numerical simulations qualitatively reproduce the experimental data from figure Fig5-10a. It is a significant revelation that distinguishes between polariton condensation and conventional lasing in weakly coupled systems, as the increase of losses in conventional lasers does not change the shape of s-curves (126), but shifts it along pump axis thereby increasing the lasing threshold, while in polariton systems the threshold and the shape of s-curve change. With this we can explain the behavior of a  $g^{(2)}(0)$  with the change of the pump spot dimensions shown in Fig.5-5g. Being under the gain saturation regime, the condensate experiences larger excessive noise due to spontaneous contribution as the stimulation is undersaturated for smaller spot sizes.

## 5.7 Microscopic Model

In this section we describe the microscopic model, first introduced in (112), used to investigate the dynamics of polariton condensates and reproduce the integral s-curves from Fig.5-10a.

We first introduce the standard Jaynes-Cummings Hamiltonian to describe the formation of exciton-polaritons in the microcavity:

$$\hat{H}_{JC} = \sum_{\mathbf{k}} \hbar\omega_{cav\mathbf{k}} \hat{a}_{cav\mathbf{k}}^+ \hat{a}_{cav\mathbf{k}} + \sum_{\mathbf{k}} \hbar\omega_{exc\mathbf{k}} \hat{c}_{exc\mathbf{k}}^+ \hat{c}_{exc\mathbf{k}} + \sum_{\mathbf{k}} \hbar\Omega_{R\mathbf{k}} (\hat{c}_{exc\mathbf{k}}^+ \hat{a}_{cav\mathbf{k}} + \hat{c}_{exc\mathbf{k}} \hat{a}_{cav\mathbf{k}}^+) \quad (5.8)$$

We then add the Fröhlich term that describes resonant interactions with the vibron subsystem of the molecules:

$$\hat{H} = \hat{H}_{JC} + \sum_{\mathbf{q}} \hbar\omega_{vib\mathbf{q}} \hat{b}_{vib\mathbf{q}}^+ \hat{b}_{vib\mathbf{q}} + \sum_{\mathbf{k}} \sum_{\mathbf{k}'} \hbar g \hat{c}_{exc\mathbf{k}}^+ \hat{c}_{exc\mathbf{k}'} \left( \hat{b}_{-(\mathbf{k}-\mathbf{k}')}^+ + \hat{b}_{(\mathbf{k}-\mathbf{k}')} \right) \quad (5.9)$$

After diagonalization of the Hamiltonian the non-hermitian processes of pumping, thermalization and dissipation are added via Lindblad superoperators. This results in the following master equation for the density matrix of upper and lower polaritons:

$$\frac{d\hat{\rho}}{dt} = \frac{i}{\hbar} \left[ \hat{\rho}, \hat{H} \right] + \hat{L}_{up}(\hat{\rho}) + \hat{L}_{low}(\hat{\rho}) + \hat{L}_{vib}(\hat{\rho}) + \hat{L}_{therm}(\hat{\rho}) + \hat{L}_{pump}(\hat{\rho}) \quad (5.10)$$

Further on we use this master equation to derive the system of differential equations for average polariton numbers in modes on lower and upper polariton branches, and adiabatically exclude the three-operator averages. After discretizing the modes on lower polariton branch in the region of interest ( $0 < k < 3\mu m^{-1}$ ) and considering the excitonic mode with energy equal to  $E_{exc} = 2.72eV$  as the pumped mode we obtain the following equations:

$$\frac{dn_p}{dt} = -\gamma_p n_p + pump(t) - G_{p \rightarrow gs} n_p (n_{gs} + 1) - G_{p \rightarrow i} n_p (n_i + D_i) \quad (5.11)$$

$$\frac{dn_{gs}}{dt} = -\gamma_{gs} n_{gs} + G_{p \rightarrow gs} n_p (n_{gs} + 1) + \sum_i \gamma_{therm} (n_i (n_{gs} + 1) - e^{-\Delta\omega/T} n_{gs} (n_i + D_i)) \quad (5.12)$$

$$\frac{dn_i}{dt} = -\gamma_i n_i + G_{p \rightarrow i} n_p (n_i + D_i) - \gamma_{therm} (n_i (n_{gs} + 1) - e^{-\Delta\omega/T} n_{gs} (n_i + D_i)) + \quad (5.13)$$

$$+ \sum_{j:\omega_j > \omega_i} \gamma_{therm} (n_j (n_i + D_i) - e^{-\Delta\omega/T} n_i (n_j + D_j)) - \sum_{j:\omega_j < \omega_i} \gamma_{therm} (n_i (n_j + D_j) - e^{-\Delta\omega/T} n_j (n_i + D_i))$$

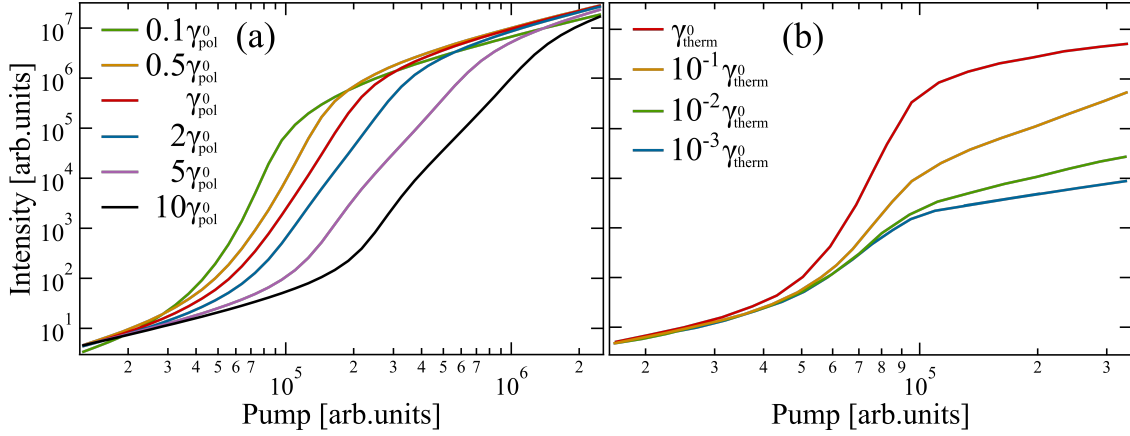


Figure 5-11: Dependencies of polariton photoluminescence intensity on pump fluence for two sets of parameters: (a) 6 different values of polariton losses  $\gamma_{pol}^0$  ( $\gamma_{therm}^0 = 10^{-6}$  is fixed). (b) 6 different values of thermalization constant  $\gamma_{therm}^0$  ( $\gamma_{pol}^0 = 3.7 meV$  is fixed).

Here  $n_p$ ,  $n_{gs}$ ,  $n_i$  are the occupancies of the pumped mode, the ground state mode and one of the  $N = 30$  modes in the region of interest on the lower polariton branch correspondingly.  $\gamma_p$ ,  $\gamma_{gs}$ ,  $\gamma_i$  are radiative losses of the same modes.  $\gamma_{therm}$  is the thermalization constant, and  $G$  are the vibron-assisted transition constants obtained from adiabatic exclusion of the vibron subsystem.

In the following section, We solve this system for different losses, described by formula (5.3).

## 5.8 Numerical Simulations

In this section we describe the numerical simulations using the equations, derived in previous Section 5.7.

We first investigate the influence of radiative losses on the shape of the s-curves. Fig5-11a shows that increasing the losses not only leads to the almost linear increase of condensation threshold (which is expected from the classic laser theory), but also to the decrease of steepness of the non-linear parts of the curves and the elongation of the transition region.

In order to understand the non-trivial change in the inclination of the s-curves both in experiment and simulations we need to take a closer look at the thermaliza-

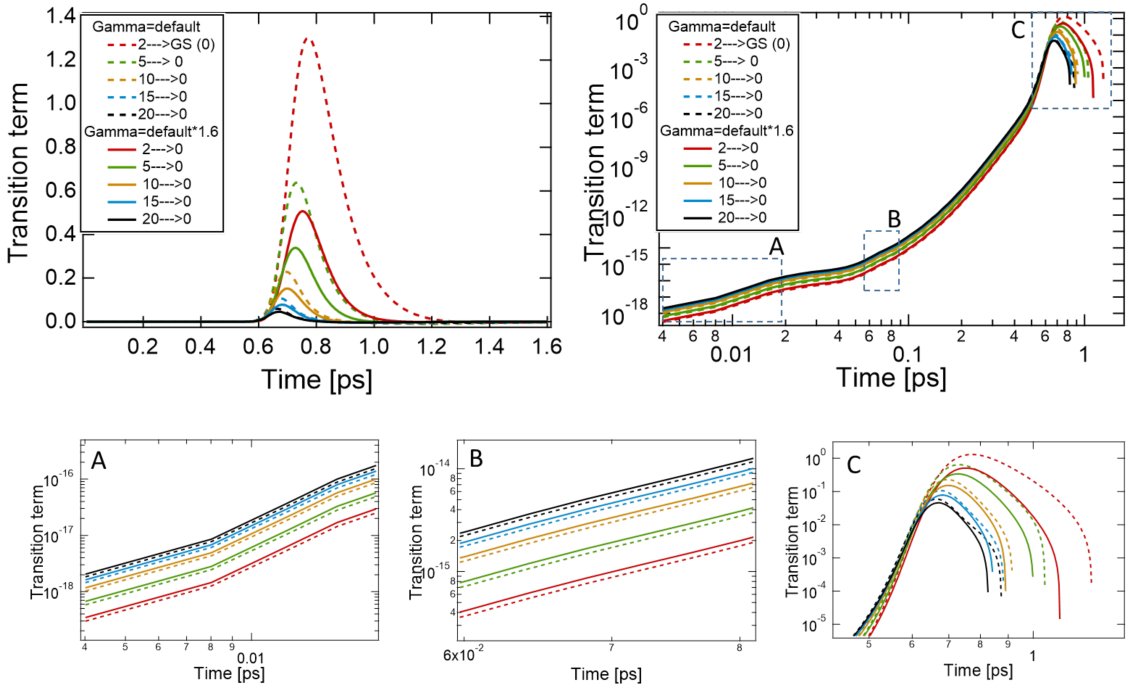


Figure 5-12: (a) Two sets of data for evolution of thermalization term  $V_{therm}^{eff} \sim n_i(n_0 + 1)\gamma_{low}^{\omega_i, \omega_0}$  in rate equations for transitions from higher ( $i=2, 5, 10, 15,$  and  $20$ ) energy states to the ground ( $j=0$ ) energy state for a 2ps pump pulse at  $\approx 3P_{th}$  for two different values of polariton losses:  $\gamma_{pol} = 3.7 \text{ meV}$  (dashed lines) and  $\gamma_{pol} = 10 \text{ meV}$  (solid lines). (b) Logarithmic scale of figure (a). (A,B,C) bottom insets are zoomed in regions from part (b) for three different time periods throughout condensation buildup: before, near, and above threshold

tion processes in the system. Mathematically the thermalization terms in equations 5.10-5.13 are the key difference from the classical laser equations. Fig5-11b shows that higher thermalization terms in the equations (with manually increased thermalization constants) result in steeper s-curves. Since these intra-LPB transition terms depend not only on the thermalization constant but also on the general occupancy of the LPB modes, it becomes clear that higher losses of the system result in smaller polariton occupancies in the above-threshold regime, which leads to slower effective thermalization and a gradual slope of the curves.

To prove the statement, we investigate the evolution of the thermalization term in the equations for two different loss parameters, Fig5-12. The dashed lines (smaller losses) in the non-linear regime are above the solid ones (higher losses), which once again shows that the effective thermalization speed is lower in the latter case.

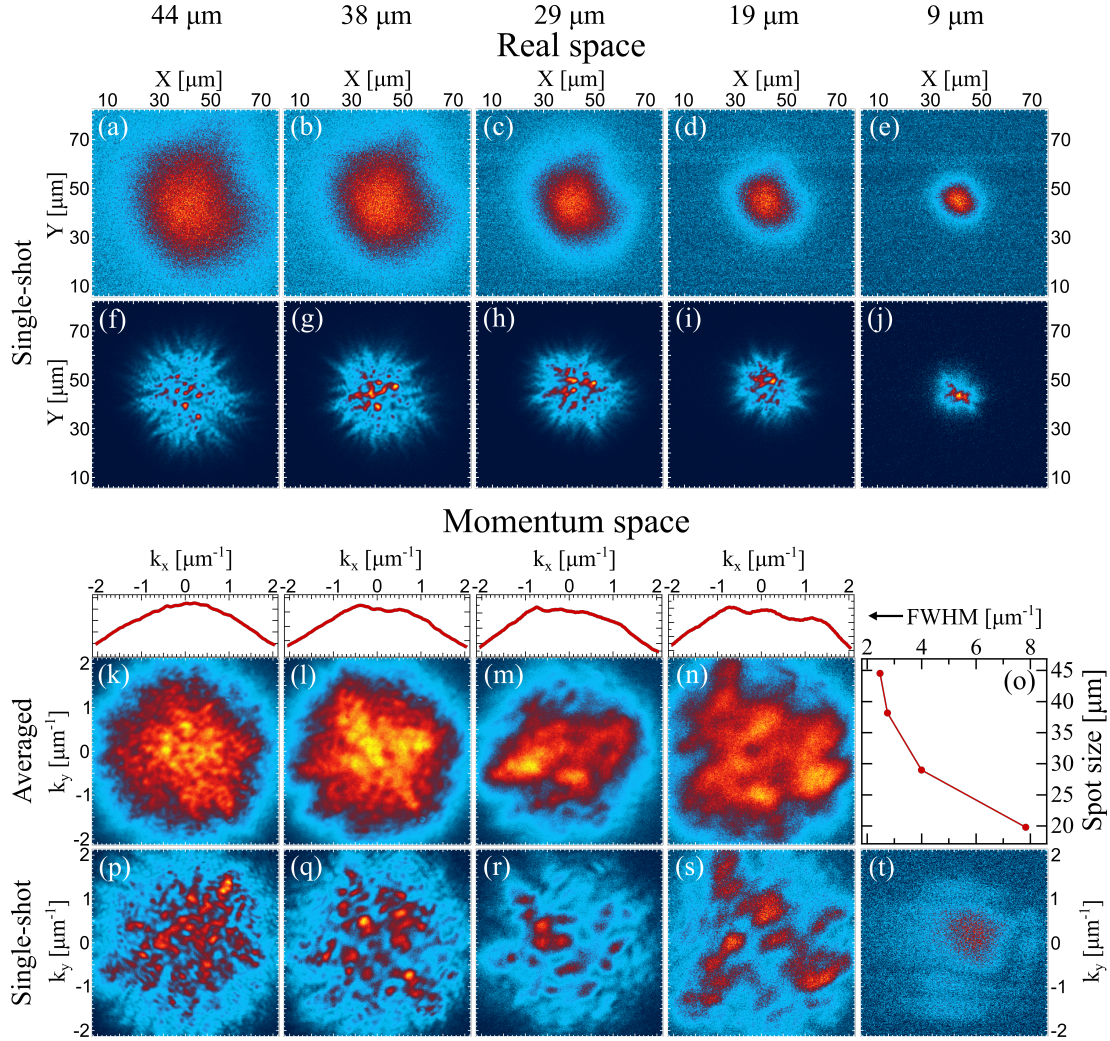


Figure 5-13: Real- and k-space polariton photoluminescence peculiarities revealed under a single-shot and an ensemble averaged imaging for different pumping spot-sizes with FWHM of  $44\mu\text{m}$ ,  $38\mu$ ,  $29\mu\text{m}$ ,  $19\mu\text{m}$ , and  $9\mu$ . (a)-(e): Single-shot real-space polariton photoluminescence below the condensation threshold for different spot-sizes. (f)-(j): Single-shot real-space polariton photoluminescence above the condensation threshold for different spot-sizes. (k)-(n): Averaged over 20 realizations k-space images of polariton photoluminescence above the condensation threshold for  $44\mu\text{m}$ ,  $38\mu\text{m}$ ,  $29\mu\text{m}$ , and  $19\mu\text{m}$  spot-sizes, respectively. Top insets show binned in  $k_y$  direction k-space PL, and (o) shows the width of these distributions (FWHM) as a function of a spot-size. (p)-(t): Single-shot k-space images of polariton photoluminescence above the condensation threshold for  $44\mu\text{m}$ ,  $38\mu$ ,  $29\mu\text{m}$ ,  $19\mu\text{m}$ , and  $9\mu\text{m}$  spot-sizes, respectively. Color scales of all images are normalized to the maxima of these images.

## 5.9 Discussion

To summarize we studied statistical, spectroscopic, and dynamic properties of the organic polariton condensate at room temperature as a function of its size. We

developed a powerful technique for detecting single condensate realization that provides access to photon statistics and allows one to study quantum statistical properties of room temperature light-matter condensates. Our findings demonstrate high degree of coherence of the condensate with a second-order correlation function  $g^{(2)}(0) = 1.00034$ . The single-shot imaging reveals the highly disordered nature of polariton condensate both in real and momentum spaces. We determined static and stochastic contributions to the condensate disorder and extracted the total shot-to-shot polariton number fluctuations as a function of the excitation spot size. Moreover, we show the disorder is independent on the system size while the photon statistics is getting broader by decreasing the system size. We explain the behavior by the kinetic nature of polaritons that starts to contribute to the losses once we enter the regime of small condensate sizes compromising intensity noise in the system. The interplay between kinetic polariton losses and thermalization defines complex non-equilibrium dynamics of polariton condensates at room temperature in sharp contrast to conventional laser behavior leading to the discrepancy in the photon statistics. From the practical point of view our results demonstrate that room temperature organic polariton condensates have relatively low intensity noise despite their non-equilibrium and disordered nature and are a promising system for various application such as polariton coherent sources, amplifiers, switches, and logic gates.

# Chapter 6

## Summary and outlook

This work started with the demonstration of ability for strongly coupled organic microcavity to undergo a polariton condensation in a quasi-steady regime, namely when condensate life-time exceeds polartion life-time for several orders of magnitude. Single-shot time resolved photolumiencence measurements were carried out, demonstrating first direct measurement of a polariton condensate life-time at room temperature. Being self-evidently essential result for the ambient polaritonics field, long-lasting condensation brings an elusive idea of an organic polariton system to reach dynamic equilibrium closer to reality and offers the possibility for devices relying on connected polariton condensates.

Further, the advantages of utilizing a hybrid metal-DBR organic microcavities for studying exciton/polariton physics were demonstrated. The first demonstration of such a system to undergo polariton condensation was reported. The system clearly has drawbacks as well. The necessity to operate in the reflection regime makes system less flexible and sophisticates the required optical design of the setup.

At last but not least, statistical, spectroscopic, and dynamic properties of the organic polariton condensate at room temperature as a function of its size were studied. Well controlled detection of single condensate realization allows for studying quantum statistical properties of room temperature light-matter condensates. Even though, the method is still to be improved, as there are several experimental challenges that might hinder pure properties of the emission such as laboratory noise, finite resolution of the photo-detectors, and EMCCD readout and background noises

that can not be completely eliminated, it provides a priceless insight on stochastic nature of highly disordered and dissipative system. From the practical point of view, these results demonstrate room temperature organic polariton condensates have relatively low intensity noise and are a promising system for various applications such as polariton coherent sources, amplifiers, switchers, and logic gates.

The author believes that this work humbly broadens the horizons of the field and suggests new directions for future studies on novel optical devices based on strong light-matter interaction.

# Bibliography

- [1] **A. D. Putintsev**, A. V. Zasedatelev, V. Y. Shishkov, M. Misko, D. Sannikov, E. S. Andrianov, Y. E. Lozovik, D. Urbonas, T. Stöferle, U. Scherf, R. F. Mahrt, and P. G. Lagoudakis, “Photon statistics of organic polariton condensates,” *under review in Physical Review X*.
- [2] **A. D. Putintsev**, A. Zasedatelev, K. E. McGhee, T. Cookson, K. Georgiou, D. Sannikov, D. G. Lidzey, and P. G. Lagoudakis, “Nano-second exciton-polariton lasing in organic microcavities,” *Applied Physics Letters*, vol. 117, no. 12, p. 123302, 2020.
- [3] K. E. McGhee, **A. D. Putintsev**, R. Jayaprakash, K. Georgiou, M. E. O’Kane, R. C. Kilbride, E. J. Cassella, M. Cavazzini, D. A. Sannikov, P. G. Lagoudakis, and D. G. Lidzey, “Polariton condensation in an organic microcavity utilising a hybrid metal-dbr mirror,” *Scientific Reports*, vol. 11, p. 20879, Oct 2021.
- [4] T. Byrnes, N. Y. Kim, and Y. Yamamoto, “Exciton–polariton condensates,” *Nature Physics*, vol. 10, pp. 803–813, 2014.
- [5] J. Kasprzak, D. D. Solnyshkov, R. André, L. S. Dang, and G. Malpuech, “Formation of an exciton polariton condensate: Thermodynamic versus kinetic regimes,” *Phys. Rev. Lett.*, vol. 101, p. 146404, Oct 2008.
- [6] S. Kéna-Cohen and S. R. Forrest, “Room-temperature polariton lasing in an organic single-crystal microcavity,” *Nature Photonics*, vol. 4, pp. 371–375, Jun 2010.
- [7] D. Ballarini, M. De Giorgi, E. Cancellieri, R. Houdré, E. Giacobino, R. Cingolani, A. Bramati, G. Gigli, and D. Sanvitto, “All-optical polariton transistor,” *Nature Communications*, vol. 4, no. 1, p. 1778, 2013.
- [8] P. G. Savvidis, J. J. Baumberg, R. M. Stevenson, M. S. Skolnick, D. M. Whittaker, and J. S. Roberts, “Angle-resonant stimulated polariton amplifier,” *Phys. Rev. Lett.*, vol. 84, pp. 1547–1550, Feb 2000.
- [9] J. D. Plumhof, T. Stöferle, L. Mai, U. Scherf, and R. F. Mahrt, “Room-temperature bose–einstein condensation of cavity exciton–polaritons in a polymer,” *Nature Materials*, vol. 13, no. 3, pp. 247–252, 2014.
- [10] D. Snoke and P. Littlewood, “Polariton condensates,” *Physics Today*, vol. 63, no. 8, pp. 42–47, 2010.

- [11] J. Keeling and N. G. Berloff, “Exciton–polariton condensation,” *Contemporary Physics*, vol. 52, no. 2, pp. 131–151, 2011.
- [12] H. Deng, G. Weihs, D. Snoke, J. Bloch, and Y. Yamamoto, “Polariton lasing vs. photon lasing in a semiconductor microcavity,” *Proceedings of the National Academy of Sciences of the United States of America*, vol. 100, pp. 15318–15323, Dec 2003. 14673089[pmid].
- [13] J. Kasprzak, M. Richard, S. Kundermann, A. Baas, P. Jeambrun, J. M. J. Keeling, F. M. Marchetti, M. H. Szymańska, R. André, J. L. Staehli, V. Savona, P. B. Littlewood, B. Deveaud, and L. S. Dang, “Bose–einstein condensation of exciton polaritons,” *Nature*, vol. 443, pp. 409–414, Sept. 2006.
- [14] E. Wertz, L. Ferrier, D. D. Solnyshkov, P. Senellart, D. Bajoni, A. Miard, A. Lemaître, G. Malpuech, and J. Bloch, “Spontaneous formation of a polariton condensate in a planar gaas microcavity,” *Applied Physics Letters*, vol. 95, no. 5, p. 051108, 2009.
- [15] A. V. Kavokin, J. J. Baumberg, G. Malpuech, and F. P. Laussy, *Microcavities*. Oxford University Press, Aug. 2017.
- [16] E. Hecht, *Optics*. Upper Saddle River, NJ: Pearson, 5 ed., Dec. 2017.
- [17] M. Maragkou, A. J. D. Grundy, T. Ostatnický, and P. G. Lagoudakis, “Longitudinal optical phonon assisted polariton laser,” *Applied Physics Letters*, vol. 97, no. 11, p. 111110, 2010.
- [18] P. G. Lagoudakis, M. D. Martin, J. J. Baumberg, A. Qarry, E. Cohen, and L. N. Pfeiffer, “Electron-polariton scattering in semiconductor microcavities,” *Phys. Rev. Lett.*, vol. 90, p. 206401, May 2003.
- [19] D. M. Coles, P. Michetti, C. Clark, W. C. Tsoi, A. M. Adawi, J.-S. Kim, and D. G. Lidzey, “Vibrationally assisted polariton-relaxation processes in strongly coupled organic-semiconductor microcavities,” *Advanced Functional Materials*, vol. 21, no. 19, pp. 3691–3696, 2011.
- [20] Y. S. Zhao, ed., *Organic Nanophotonics; Fundamentals and Applications*. Nano-Optics and Nanophotonics, New York, NY: Springer, Jan. 2014.
- [21] A. Strashko, P. Kirton, and J. Keeling, “Organic polariton lasing and the weak to strong coupling crossover,” *Phys. Rev. Lett.*, vol. 121, p. 193601, Nov 2018.
- [22] A. Kavokin, J. J. Baumberg, G. Malpuech, and F. P. Laussy, *Microcavities*. Oxford University Press, 12 2007.
- [23] H. Deng, H. Haug, and Y. Yamamoto, “Exciton-polariton bose-einstein condensation,” *Rev. Mod. Phys.*, vol. 82, pp. 1489–1537, May 2010.
- [24] K. S. Daskalakis, S. A. Maier, R. Murray, and S. Kéna-Cohen, “Nonlinear interactions in an organic polariton condensate,” *Nature Materials*, vol. 13, pp. 271–278, Feb. 2014.

- [25] K. Georgiou, R. Jayaprakash, A. Askitopoulos, D. M. Coles, P. G. Lagoudakis, and D. G. Lidzey, "Generation of anti-stokes fluorescence in a strongly coupled organic semiconductor microcavity," *ACS Photonics*, vol. 5, pp. 4343–4351, Nov 2018.
- [26] A. V. Zasedatelev, A. V. Baranikov, D. Urbonas, F. Scafrimuto, U. Scherf, T. Stöferle, R. F. Mahrt, and P. G. Lagoudakis, "A room-temperature organic polariton transistor," *Nature Photonics*, vol. 13, pp. 378–383, Mar. 2019.
- [27] T. Yagafarov, D. Sannikov, A. Zasedatelev, K. Georgiou, A. Baranikov, O. Kyriienko, I. Shelykh, L. Gai, Z. Shen, D. Lidzey, and P. Lagoudakis, "Mechanisms of blueshifts in organic polariton condensates," *Communications Physics*, vol. 3, p. 18, Jan 2020.
- [28] D. Sanvitto and S. Kéna-Cohen, "The road towards polaritonic devices," *Nature Materials*, vol. 15, pp. 1061–1073, July 2016.
- [29] L. Pitaevskii and S. Stringari, *Bose-Einstein Condensation and Superfluidity*. Oxford University Press, 01 2016.
- [30] J. Keeling and S. Kéna-Cohen, "Bose–einstein condensation of exciton-polaritons in organic microcavities," *Annual Review of Physical Chemistry*, vol. 71, no. 1, pp. 435–459, 2020. PMID: 32126177.
- [31] D. G. Lidzey, D. D. C. Bradley, M. S. Skolnick, T. Virgili, S. Walker, and D. M. Whittaker, "Strong exciton–photon coupling in an organic semiconductor microcavity," *Nature*, vol. 395, pp. 53–55, Sep 1998.
- [32] D. G. Lidzey, D. D. C. Bradley, T. Virgili, A. Armitage, M. S. Skolnick, and S. Walker, "Room temperature polariton emission from strongly coupled organic semiconductor microcavities," *Phys. Rev. Lett.*, vol. 82, pp. 3316–3319, Apr 1999.
- [33] R. J. Holmes and S. R. Forrest, "Strong exciton-photon coupling and exciton hybridization in a thermally evaporated polycrystalline film of an organic small molecule," *Physical Review Letters*, vol. 93, Oct. 2004.
- [34] C.-C. Wu, Y.-T. Lin, K.-T. Wong, R.-T. Chen, and Y.-Y. Chien, "Efficient organic blue-light-emitting devices with double confinement on terfluorenes with ambipolar carrier transport properties," *Advanced Materials*, vol. 16, no. 1, pp. 61–65, 2004.
- [35] T. Cookson, K. Georgiou, A. Zasedatelev, R. T. Grant, T. Virgili, M. Cavazzini, F. Galeotti, C. Clark, N. G. Berloff, D. G. Lidzey, and P. G. Lagoudakis, "A yellow polariton condensate in a dye filled microcavity," *Advanced Optical Materials*, vol. 5, p. 1700203, July 2017.
- [36] K. E. McGhee, R. Jayaprakash, K. Georgiou, S. L. Burg, and D. G. Lidzey, "Polariton condensation in a microcavity using a highly-stable molecular dye," *Journal of Materials Chemistry C*, vol. 10, no. 11, pp. 4187–4195, 2022.

- [37] A. B. Cubitt, R. Heim, S. R. Adams, A. E. Boyd, L. A. Gross, and R. Y. Tsien, "Understanding, improving and using green fluorescent proteins," *Trends in Biochemical Sciences*, vol. 20, pp. 448–455, Nov. 1995.
- [38] C. P. Dietrich, A. Steude, L. Tropsch, M. Schubert, N. M. Kronenberg, K. Ostermann, S. Höfling, and M. C. Gather, "An exciton-polariton laser based on biologically produced fluorescent protein," *Science Advances*, vol. 2, no. 8, 2016.
- [39] S. Betzold, M. Dusel, O. Kyriienko, C. P. Dietrich, S. Klemmt, J. Ohmer, U. Fischer, I. A. Shelykh, C. Schneider, and S. Höfling, "Coherence and interaction in confined room-temperature polariton condensates with frenkel excitons," *ACS Photonics*, vol. 7, pp. 384–392, Dec. 2019.
- [40] F. Scafirimuto, D. Urbonas, U. Scherf, R. F. Mahrt, and T. Stöferle, "Room-temperature exciton-polariton condensation in a tunable zero-dimensional microcavity," *ACS Photonics*, vol. 5, no. 1, pp. 85–89, 2018.
- [41] D. Sannikov, T. Yagafarov, K. Georgiou, A. Zasedatelev, A. Baranikov, L. Gai, Z. Shen, D. Lidzey, and P. Lagoudakis, "Room temperature broadband polariton lasing from a dye-filled microcavity," *Advanced Optical Materials*, vol. 7, no. 17, p. 1900163, 2019.
- [42] S. K. Rajendran, M. Wei, H. Ohadi, A. Ruseckas, G. A. Turnbull, and I. D. W. Samuel, "Low threshold polariton lasing from a solution-processed organic semiconductor in a planar microcavity," *Advanced Optical Materials*, vol. 7, no. 12, p. 1801791, 2019.
- [43] M. Wei, S. K. Rajendran, H. Ohadi, L. Tropsch, M. C. Gather, G. A. Turnbull, and I. D. W. Samuel, "Low-threshold polariton lasing in a highly disordered conjugated polymer," *Optica*, vol. 6, p. 1124, Aug. 2019.
- [44] A. V. Zasedatelev, A. V. Baranikov, D. Urbonas, F. Scafirimuto, U. Scherf, T. Stöferle, R. F. Mahrt, and P. G. Lagoudakis, "A room-temperature organic polariton transistor," *Nature Photonics*, vol. 13, no. 6, pp. 378–383, 2019.
- [45] A. V. Baranikov, A. V. Zasedatelev, D. Urbonas, F. Scafirimuto, U. Scherf, T. Stöferle, R. F. Mahrt, and P. G. Lagoudakis, "All-optical cascable universal logic gate with sub-picosecond operation," 2020.
- [46] A. Zasedatelev, A. V. Baranikov, D. Sannikov, D. Urbonas, F. Scafirimuto, V. Y. Shishkov, E. S. Andrianov, Y. E. Lozovik, U. Scherf, T. Stöferle, R. F. Mahrt, and P. G. Lagoudakis, "Organic single-photon switch," 2020.
- [47] A. J. Musser, S. K. Rajendran, K. Georgiou, L. Gai, R. T. Grant, Z. Shen, M. Cavazzini, A. Ruseckas, G. A. Turnbull, I. D. W. Samuel, J. Clark, and D. G. Lidzey, "Intermolecular states in organic dye dispersions: excimers vs. aggregates," *J. Mater. Chem. C*, vol. 5, pp. 8380–8389, 2017.

- [48] R. T. Grant, P. Michetti, A. J. Musser, P. Gregoire, T. Virgili, E. Vella, M. Cavazzini, K. Georgiou, F. Galeotti, C. Clark, J. Clark, C. Silva, and D. G. Lidzey, "Efficient radiative pumping of polaritons in a strongly coupled microcavity by a fluorescent molecular dye," *Advanced Optical Materials*, vol. 4, no. 10, pp. 1615–1623, 2016.
- [49] K. Georgiou, P. Michetti, L. Gai, M. Cavazzini, Z. Shen, and D. G. Lidzey, "Control over energy transfer between fluorescent bodipy dyes in a strongly coupled microcavity," *ACS Photonics*, vol. 5, no. 1, pp. 258–266, 2018.
- [50] B. Liu, R. Wu, and V. M. Menon, "Propagating hybrid tamm exciton polaritons in organic microcavity," *The Journal of Physical Chemistry C*, vol. 123, no. 43, pp. 26509–26515, 2019.
- [51] V. Savona, L. Andreani, P. Schwendimann, and A. Quattropani, "Quantum well excitons in semiconductor microcavities: Unified treatment of weak and strong coupling regimes," *Solid State Communications*, vol. 93, no. 9, pp. 733 – 739, 1995.
- [52] T.-C. Lu, Y.-Y. Lai, Y.-P. Lan, S.-W. Huang, J.-R. Chen, Y.-C. Wu, W.-F. Hsieh, and H. Deng, "Room temperature polariton lasing vs. photon lasing in a zno-based hybrid microcavity," *Opt. Express*, vol. 20, pp. 5530–5537, Feb 2012.
- [53] G. G. Paschos, N. Somaschi, S. I. Tsintzos, D. Coles, J. L. Bricks, Z. Hatzopoulos, D. G. Lidzey, P. G. Lagoudakis, and P. G. Savvidis, "Hybrid organic-inorganic polariton laser," *Scientific Reports*, vol. 7, p. 11377, Sep 2017.
- [54] A. I. Tartakovskii, M. Emam-Ismael, D. G. Lidzey, M. S. Skolnick, D. D. C. Bradley, S. Walker, and V. M. Agranovich, "Raman scattering in strongly coupled organic semiconductor microcavities," *Phys. Rev. B*, vol. 63, p. 121302, Mar 2001.
- [55] D. M. Coles, P. Michetti, C. Clark, W. C. Tsoi, A. M. Adawi, J.-S. Kim, and D. G. Lidzey, "Vibrationally assisted polariton-relaxation processes in strongly coupled organic-semiconductor microcavities," *Advanced Functional Materials*, vol. 21, no. 19, pp. 3691–3696, 2011.
- [56] N. Somaschi, L. Mouchliadis, D. Coles, I. E. Perakis, D. G. Lidzey, P. G. Lagoudakis, and P. G. Savvidis, "Ultrafast polariton population build-up mediated by molecular phonons in organic microcavities," *Applied Physics Letters*, vol. 99, no. 14, p. 143303, 2011.
- [57] K. S. Daskalakis, S. A. Maier, and S. Kéna-Cohen, "Spatial coherence and stability in a disordered organic polariton condensate," *Phys. Rev. Lett.*, vol. 115, p. 035301, Jul 2015.
- [58] N. Bobrovska, M. Matuszewski, K. S. Daskalakis, S. A. Maier, and S. Kéna-Cohen, "Dynamical instability of a nonequilibrium exciton-polariton condensate," *ACS Photonics*, vol. 5, no. 1, pp. 111–118, 2018.

- [59] I. Carusotto and C. Ciuti, “Quantum fluids of light,” *Rev. Mod. Phys.*, vol. 85, pp. 299–366, Feb 2013.
- [60] G. Lerario, A. Fieramosca, F. Barachati, D. Ballarini, K. S. Daskalakis, L. Dominici, M. D. Giorgi, S. A. Maier, G. Gigli, S. Kéna-Cohen, and D. Sanvitto, “Room-temperature superfluidity in a polariton condensate,” *Nature Physics*, vol. 13, pp. 837–841, June 2017.
- [61] M. Dusel, S. Betzold, O. A. Egorov, S. Klemmt, J. Ohmer, U. Fischer, S. Höfling, and C. Schneider, “Room temperature organic exciton-polariton condensate in a lattice,” 2019.
- [62] T. Gao, P. S. Eldridge, T. C. H. Liew, S. I. Tsintzos, G. Stavriniadis, G. Deligeorgis, Z. Hatzopoulos, and P. G. Savvidis, “Polariton condensate transistor switch,” *Phys. Rev. B*, vol. 85, p. 235102, Jun 2012.
- [63] H. S. Nguyen, D. Vishnevsky, C. Sturm, D. Tanese, D. Solnyshkov, E. Galopin, A. Lemaître, I. Sagnes, A. Amo, G. Malpuech, and J. Bloch, “Realization of a double-barrier resonant tunneling diode for cavity polaritons,” *Phys. Rev. Lett.*, vol. 110, p. 236601, Jun 2013.
- [64] C. Sturm, D. Tanese, H. S. Nguyen, H. Flayac, E. Galopin, A. Lemaître, I. Sagnes, D. Solnyshkov, A. Amo, G. Malpuech, and J. Bloch, “All-optical phase modulation in a cavity-polariton mach–zehnder interferometer,” *Nature Communications*, vol. 5, no. 1, p. 3278, 2014.
- [65] F. Marsault, H. S. Nguyen, D. Tanese, A. Lemaître, E. Galopin, I. Sagnes, A. Amo, and J. Bloch, “Realization of an all optical exciton-polariton router,” *Applied Physics Letters*, vol. 107, no. 20, p. 201115, 2015.
- [66] P. A. Hobson, W. L. Barnes, D. G. Lidzey, G. A. Gehring, D. M. Whittaker, M. S. Skolnick, and S. Walker, “Strong exciton–photon coupling in a low- $q$  all-metal mirror microcavity,” *Applied Physics Letters*, vol. 81, pp. 3519–3521, Nov. 2002.
- [67] T. Schwartz, J. A. Hutchison, J. Léonard, C. Genet, S. Haacke, and T. W. Ebbesen, “Polariton dynamics under strong light–molecule coupling,” *ChemPhysChem*, vol. 14, no. 1, pp. 125–131, 2013.
- [68] S. Kéna-Cohen, S. A. Maier, and D. D. C. Bradley, “Ultrastrongly coupled exciton–polaritons in metal-clad organic semiconductor microcavities,” *Advanced Optical Materials*, vol. 1, no. 11, pp. 827–833, 2013.
- [69] B. Liu, P. Rai, J. Grezimak, R. J. Twieg, and K. D. Singer, “Coupling of exciton-polaritons in low  $-q$  coupled microcavities beyond the rotating wave approximation,” *Phys. Rev. B*, vol. 92, p. 155301, Oct 2015.
- [70] Y. Obara, K. Saitoh, M. Oda, and T. Tani, “Room-temperature fluorescence lifetime of pseudoisocyanine (PIC) J excitons with various aggregate morphologies in relation to microcavity polariton formation,” *Int J Mol Sci*, vol. 13, pp. 5851–5865, May 2012.

- [71] D. M. Coles, R. T. Grant, D. G. Lidzey, C. Clark, and P. G. Lagoudakis, “Imaging the polariton relaxation bottleneck in strongly coupled organic semiconductor microcavities,” *Phys. Rev. B*, vol. 88, p. 121303, Sep 2013.
- [72] R. P. Sabatini, B. Zhang, A. Gupta, J. Leoni, W. W. H. Wong, and G. Lakhwani, “Molecularly isolated perylene diimides enable both strong exciton–photon coupling and high photoluminescence quantum yield,” *Journal of Materials Chemistry C*, vol. 7, no. 10, pp. 2954–2960, 2019.
- [73] D. M. Coles, Q. Chen, L. C. Flatten, J. M. Smith, K. Müllen, A. Narita, and D. G. Lidzey, “Strong exciton–photon coupling in a nanographene filled microcavity,” *Nano Letters*, vol. 17, pp. 5521–5525, Sep 2017.
- [74] L. G. Connolly, D. G. Lidzey, R. Butté, A. M. Adawi, D. M. Whittaker, M. S. Skolnick, and R. Airey, “Strong coupling in high-finesse organic semiconductor microcavities,” *Applied Physics Letters*, vol. 83, no. 26, pp. 5377–5379, 2003.
- [75] T. Virgili, D. Coles, A. M. Adawi, C. Clark, P. Michetti, S. K. Rajendran, D. Brida, D. Polli, G. Cerullo, and D. G. Lidzey, “Ultrafast polariton relaxation dynamics in an organic semiconductor microcavity,” *Phys. Rev. B*, vol. 83, p. 245309, Jun 2011.
- [76] V. D. Kulakovskii, A. V. Larionov, S. I. Novikov, S. Höfling, C. Schneider, and A. Forchel, “Bose-einstein condensation of exciton polaritons in high-q planar microcavities with GaAs quantum wells,” *JETP Letters*, vol. 92, pp. 595–599, Nov 2010.
- [77] P. Tsotsis, P. S. Eldridge, T. Gao, S. I. Tsintzos, Z. Hatzopoulos, and P. G. Savvidis, “Lasing threshold doubling at the crossover from strong to weak coupling regime in GaAs microcavity,” *New Journal of Physics*, vol. 14, p. 023060, feb 2012.
- [78] R. Jayaprakash, C. E. Whittaker, K. Georgiou, O. S. Game, K. E. McGhee, D. M. Coles, and D. G. Lidzey, “Two-dimensional organic-exciton polariton lattice fabricated using laser patterning,” *ACS Photonics*, vol. 7, pp. 2273–2281, Aug 2020.
- [79] S.-C. Wang, T.-C. Lu, C.-C. Kao, J.-T. Chu, G.-S. Huang, H.-C. Kuo, S.-W. Chen, T.-T. Kao, J.-R. Chen, and L.-F. Lin, “Optically pumped GaN-based vertical cavity surface emitting lasers: Technology and characteristics,” *Japanese Journal of Applied Physics*, vol. 46, pp. 5397–5407, aug 2007.
- [80] K. S. Daskalakis, S. A. Maier, and S. Kéna-Cohen, “Spatial coherence and stability in a disordered organic polariton condensate,” *Phys. Rev. Lett.*, vol. 115, p. 035301, Jul 2015.
- [81] G. M. Akselrod, E. R. Young, K. W. Stone, A. Palatnik, V. Bulović, and Y. R. Tischler, “Reduced lasing threshold from organic dye microcavities,” *Phys. Rev. B*, vol. 90, p. 035209, Jul 2014.

- [82] R. Jayaprakash, F. G. Kalaitzakis, G. Christmann, K. Tsagaraki, M. Hocevar, B. Gayral, E. Monroy, and N. T. Pelekanos, “Ultra-low threshold polariton lasing at room temperature in a gan membrane microcavity with a zero-dimensional trap,” *Scientific Reports*, vol. 7, p. 5542, Jul 2017.
- [83] F. Scafrimuto, D. Urbonas, M. A. Becker, U. Scherf, R. F. Mahrt, and T. Stöferle, “Tunable exciton–polariton condensation in a two-dimensional lieb lattice at room temperature,” *Communications Physics*, vol. 4, p. 39, Mar 2021.
- [84] A. Perrin, R. Bücker, S. Manz, T. Betz, C. Koller, T. Plisson, T. Schumm, and J. Schmiedmayer, “Hanbury brown and twiss correlations across the bose–einstein condensation threshold,” *Nature Physics*, vol. 8, pp. 195–198, Jan. 2012.
- [85] A. Öttl, S. Ritter, M. Köhl, and T. Esslinger, “Correlations and counting statistics of an atom laser,” *Phys. Rev. Lett.*, vol. 95, p. 090404, Aug 2005.
- [86] G. Lerario, D. Ballarini, A. Fieramosca, A. Cannavale, A. Genco, F. Mangione, S. Gambino, L. Dominici, M. D. Giorgi, G. Gigli, and D. Sanvitto, “High-speed flow of interacting organic polaritons,” *Light: Science & Applications*, vol. 6, pp. e16212–e16212, Sept. 2016.
- [87] E. Estrecho, T. Gao, N. Bobrovska, M. D. Fraser, M. Steger, L. Pfeiffer, K. West, T. C. H. Liew, M. Matuszewski, D. W. Snoke, A. G. Truscott, and E. A. Ostrovskaya, “Single-shot condensation of exciton polaritons and the hole burning effect,” *Nature Communications*, vol. 9, p. 2944, Aug 2018.
- [88] N. Bobrovska, M. Matuszewski, K. S. Daskalakis, S. A. Maier, and S. Kéna-Cohen, “Dynamical instability of a nonequilibrium exciton-polariton condensate,” *ACS Photonics*, vol. 5, pp. 111–118, Aug. 2017.
- [89] Y. Sun, P. Wen, Y. Yoon, G. Liu, M. Steger, L. N. Pfeiffer, K. West, D. W. Snoke, and K. A. Nelson, “Bose-einstein condensation of long-lifetime polaritons in thermal equilibrium,” *Phys. Rev. Lett.*, vol. 118, p. 016602, Jan 2017.
- [90] A. Genco, A. Ridolfo, S. Savasta, S. Patanè, G. Gigli, and M. Mazzeo, “Bright polariton coumarin-based OLEDs operating in the ultrastrong coupling regime,” *Advanced Optical Materials*, vol. 6, p. 1800364, June 2018.
- [91] S. Shen, W. Yang, J. Shan, G. Sun, T.-M. Shih, Y. Zhou, and Z. Yang, “Multiband enhanced second-harmonic generation via plasmon hybridization,” *The Journal of Chemical Physics*, vol. 153, p. 151102, Oct. 2020.
- [92] J. D. Plumhof, T. Stöferle, L. Mai, U. Scherf, and R. F. Mahrt, “Room-temperature bose–einstein condensation of cavity exciton–polaritons in a polymer,” *Nature Materials*, vol. 13, pp. 247–252, Dec. 2013.
- [93] P. Schwendimann and A. Quattropani, “Statistics of the polariton condensate,” *Phys. Rev. B*, vol. 77, p. 085317, Feb 2008.

- [94] F. P. Laussy, G. Malpuech, A. Kavokin, and P. Bigenwald, “Spontaneous coherence buildup in a polariton laser,” *Phys. Rev. Lett.*, vol. 93, p. 016402, Jun 2004.
- [95] D. Sarchi and V. Savona, “Spectrum and thermal fluctuations of a microcavity polariton bose-einstein condensate,” *Phys. Rev. B*, vol. 77, p. 045304, Jan 2008.
- [96] M. Wouters and V. Savona, “Stochastic classical field model for polariton condensates,” *Phys. Rev. B*, vol. 79, p. 165302, Apr 2009.
- [97] A. Askitopoulos, L. Pickup, S. Alyatkin, A. Zasedatelev, K. G. Lagoudakis, W. Langbein, and P. G. Lagoudakis, “Giant increase of temporal coherence in optically trapped polariton condensate,” 2019.
- [98] D. Sarchi and V. Savona, “Long-range order in the bose-einstein condensation of polaritons,” *Phys. Rev. B*, vol. 75, p. 115326, Mar 2007.
- [99] M. Pieczarka, E. Estrecho, M. Boozarjmehr, O. Bleu, M. Steger, K. West, L. N. Pfeiffer, D. W. Snoke, J. Levinsen, M. M. Parish, A. G. Truscott, and E. A. Ostrovskaya, “Observation of quantum depletion in a non-equilibrium exciton–polariton condensate,” *Nature Communications*, vol. 11, p. 429, Jan 2020.
- [100] S. Baryshev, A. Zasedatelev, H. Sigurdsson, I. Gnusov, J. D. Töpfer, A. Askitopoulos, and P. G. Lagoudakis, “Engineering photon statistics in a spinor polariton condensate,” *Phys. Rev. Lett.*, vol. 128, p. 087402, Feb 2022.
- [101] A. H. Safavi-Naeini, J. Chan, J. T. Hill, S. Gröblacher, H. Miao, Y. Chen, M. Aspelmeyer, and O. Painter, “Laser noise in cavity-optomechanical cooling and thermometry,” *New Journal of Physics*, vol. 15, p. 035007, Mar. 2013.
- [102] C. M. Caves, “Quantum-mechanical noise in an interferometer,” *Physical Review D*, vol. 23, pp. 1693–1708, Apr. 1981.
- [103] C. Schneider, A. Rahimi-Iman, N. Y. Kim, J. Fischer, I. G. Savenko, M. Amthor, M. Lermer, A. Wolf, L. Worschech, V. D. Kulakovskii, I. A. Shelykh, M. Kamp, S. Reitzenstein, A. Forchel, Y. Yamamoto, and S. Höfling, “An electrically pumped polariton laser,” *Nature*, vol. 497, pp. 348–352, May 2013.
- [104] N. G. Berloff, M. Silva, K. Kalinin, A. Askitopoulos, J. D. Töpfer, P. Cilibrizzi, W. Langbein, and P. G. Lagoudakis, “Realizing the classical XY hamiltonian in polariton simulators,” *Nature Materials*, vol. 16, pp. 1120–1126, Sept. 2017.
- [105] S. Klemmt, T. H. Harder, O. A. Egorov, K. Winkler, R. Ge, M. A. Bandres, M. Emmerling, L. Worschech, T. C. H. Liew, M. Segev, C. Schneider, and S. Höfling, “Exciton-polariton topological insulator,” *Nature*, vol. 562, pp. 552–556, Oct. 2018.

- [106] A. Delteil, T. Fink, A. Schade, S. Höfling, C. Schneider, and A. İmamoğlu, “Towards polariton blockade of confined exciton–polaritons,” *Nature Materials*, vol. 18, pp. 219–222, Feb. 2019.
- [107] G. Muñoz-Matutano, A. Wood, M. Johnsson, X. Vidal, B. Q. Baragiola, A. Reinhard, A. Lemaître, J. Bloch, A. Amo, G. Nogues, B. Besga, M. Richard, and T. Volz, “Emergence of quantum correlations from interacting fibre-cavity polaritons,” *Nature Materials*, vol. 18, pp. 213–218, Feb. 2019.
- [108] J. D. Töpfer, H. Sigurdsson, L. Pickup, and P. G. Lagoudakis, “Time-delay polaritonics,” *Communications Physics*, vol. 3, p. 2, Jan 2020.
- [109] S. Harrison, H. Sigurdsson, S. Alyatkin, J. Töpfer, and P. Lagoudakis, “Solving the max-3-cut problem with coherent networks,” *Phys. Rev. Applied*, vol. 17, p. 024063, Feb 2022.
- [110] D. Ballarini, A. Gianfrate, R. Panico, A. Opala, S. Ghosh, L. Dominici, V. Ardizzone, M. D. Giorgi, G. Lerario, G. Gigli, T. C. H. Liew, M. Matuszewski, and D. Sanvitto, “Polaritonic neuromorphic computing outperforms linear classifiers,” *Nano Letters*, vol. 20, pp. 3506–3512, Apr. 2020.
- [111] R. Mirek, A. Opala, P. Comaron, M. Furman, M. Król, K. Tyszka, B. Seredyński, D. Ballarini, D. Sanvitto, T. C. H. Liew, W. Pacuski, J. Sufczyński, J. Szczytko, M. Matuszewski, and B. Piętka, “Neuromorphic binarized polariton networks,” *Nano Letters*, vol. 21, pp. 3715–3720, Feb. 2021.
- [112] A. V. Zasedatelev, A. V. Baranikov, D. Sannikov, D. Urbonas, F. Scafirimuto, V. Y. Shishkov, E. S. Andrianov, Y. E. Lozovik, U. Scherf, T. Stöferle, R. F. Mahrt, and P. G. Lagoudakis, “Single-photon nonlinearity at room temperature,” *Nature*, vol. 597, pp. 493–497, Sept. 2021.
- [113] V. Y. Shishkov, E. S. Andrianov, A. V. Zasedatelev, P. G. Lagoudakis, and Y. E. Lozovik, “Exact analytical solution for the density matrix of a nonequilibrium polariton bose-einstein condensate,” *Phys. Rev. Lett.*, vol. 128, p. 065301, Feb 2022.
- [114] A. P. D. Love, D. N. Krizhanovskii, D. M. Whittaker, R. Bouchekioua, D. Sanvitto, S. A. Rizeiqi, R. Bradley, M. S. Skolnick, P. R. Eastham, R. André, and L. S. Dang, “Intrinsic decoherence mechanisms in the microcavity polariton condensate,” *Phys. Rev. Lett.*, vol. 101, p. 067404, Aug 2008.
- [115] J. Wiersig, C. Gies, F. Jahnke, M. Aßmann, T. Berstermann, M. Bayer, C. Kistner, S. Reitzenstein, C. Schneider, S. Höfling, A. Forchel, C. Kruse, J. Kalden, and D. Hommel, “Direct observation of correlations between individual photon emission events of a microcavity laser,” *Nature*, vol. 460, pp. 245–249, July 2009.
- [116] M. Aßmann, F. Veit, M. Bayer, M. van der Poel, and J. M. Hvam, “Higher-order photon bunching in a semiconductor microcavity,” *Science*, vol. 325, pp. 297–300, July 2009.

- [117] A. F. Adiyatullin, M. D. Anderson, P. V. Busi, H. Abbaspour, R. André, M. T. Portella-Oberli, and B. Deveaud, “Temporally resolved second-order photon correlations of exciton-polariton bose-einstein condensate formation,” *Applied Physics Letters*, vol. 107, p. 221107, Nov. 2015.
- [118] F. Scafirimuto, D. Urbonas, U. Scherf, R. F. Mahrt, and T. Stöferle, “Room-temperature exciton-polariton condensation in a tunable zero-dimensional microcavity,” *ACS Photonics*, vol. 5, pp. 85–89, Oct. 2017.
- [119] B. Schweitzer, G. Wegmann, D. Hertel, R. F. Mahrt, H. Bässler, F. Uckert, U. Scherf, and K. Müllen, “Spontaneous and stimulated emission from a ladder-type conjugated polymer,” *Physical Review B*, vol. 59, pp. 4112–4118, Feb. 1999.
- [120] S. Kim, B. Zhang, Z. Wang, J. Fischer, S. Brodbeck, M. Kamp, C. Schneider, S. Höfling, and H. Deng, “Coherent polariton laser,” *Phys. Rev. X*, vol. 6, p. 011026, Mar 2016.
- [121] C. Gardiner, P. Zoller, and P. Zoller, *Quantum Noise: A Handbook of Markovian and Non-Markovian Quantum Stochastic Methods with Applications to Quantum Optics*. Springer Series in Synergetics, Springer, 2004.
- [122] D. Porras and C. Tejedor, “Linewidth of a polariton laser: Theoretical analysis of self-interaction effects,” *Phys. Rev. B*, vol. 67, p. 161310, Apr 2003.
- [123] G. Nardin, K. G. Lagoudakis, M. Wouters, M. Richard, A. Baas, R. André, L. S. Dang, B. Pietka, and B. Deveaud-Plédran, “Dynamics of long-range ordering in an exciton-polariton condensate,” *Phys. Rev. Lett.*, vol. 103, p. 256402, Dec 2009.
- [124] D. W. Snoke and J. P. Wolfe, “Population dynamics of a bose gas near saturation,” *Physical Review B*, vol. 39, pp. 4030–4037, Mar. 1989.
- [125] V. V. Belykh, N. N. Sibeldin, V. D. Kulakovskii, M. M. Glazov, M. A. Semina, C. Schneider, S. Höfling, M. Kamp, and A. Forchel, “Coherence expansion and polariton condensate formation in a semiconductor microcavity,” *Phys. Rev. Lett.*, vol. 110, p. 137402, Mar 2013.
- [126] P. R. Rice and H. J. Carmichael, “Photon statistics of a cavity-QED laser: A comment on the laser–phase-transition analogy,” vol. 50, pp. 4318–4329, Nov. 1994.